Second release of the CoRe database of binary neutron star merger waveforms

Alejandra Gonzalez [1], Francesco Zappa [1], Matteo Breschi [1], Sebastiano Bernuzzi [1], David Radice [2,3,4], Ananya Adhikari [5], Alessandro Camilletti [6,7], Swami Vivekanandji Chaurasia [8], Georgios Doulis [1,9], Surendra Padamata [2,3], Alireza Rashti[2,3], Maximiliano Ujevic [10], Bernd Brügmann [1], William Cook [1], Tim Dietrich [11,12], Albino Perego [6,7], Amit Poudel [5], Wolfgang Tichy [5]

[1]Theoretisch-Physikalisches Institut, Friedrich-Schiller-Universität Jena, 07743, Jena, Germany
[2]Institute for Gravitation & the Cosmos, The Pennsylvania State University, University Park PA 16802, USA
[3]Department of Physics, The Pennsylvania State University, University Park PA 16802, USA
[4]Department of Astronomy & Astrophysics, The Pennsylvania State University, University Park PA 16802, USA
[5]Department of Physics, Florida Atlantic University, Boca Raton, FL 33431, USA
[6]Dipartimento di Fisica, Universitá di Trento, via Sommarive 14, 38123 Trento, Italy
[7]INFN-TIFPA, Trento Institute for Fundamental Physics and Applications, via Sommarive 14, 38123 Trento, Italy
[8]The Oskar Klein Centre, Department of Astronomy, Stockholm University, AlbaNova, SE-10691 Stockholm, Sweden
[9]Department of Physics, University of Athens, 15783, Athens, Greece
[10]Centro de Ciências Naturais e Humanas, Universidade Federal do ABC, 09210-170, Santo André, São Paulo, Brazil
[11]Institut für Physik und Astronomie, Universität Potsdam, Haus 28, Karl-Liebknecht-Str. 24/25, 14476, Potsdam, Germany
[12]Max Planck Institute for Gravitational Physics (Albert Einstein Institute), Am Mühlenberg 1, Potsdam, Germany

1 November 2022

Abstract. We present the second data release of gravitational waveforms from binary neutron star merger simulations performed by the Computational Relativity (CoRe) collaboration. The current database consists of 254 different binary neutron star configurations and a total of 590 individual numerical-relativity simulations using various grid resolutions. The released waveform data contain the strain and the Weyl curvature multipoles up to $\ell = m = 4$. They span a significant portion of the mass, mass-ratio, spin and eccentricity parameter space and include targeted configurations to the events GW170817 and GW190425. CoRe simulations are performed with 18 different equations of state, seven of which are finite temperature models, and three of which account for non-hadronic degrees of freedom. About half of the released data

are computed with high-order hydrodynamics schemes for tens of orbits to merger; the other half is computed with advanced microphysics. We showcase a standard waveform error analysis and discuss the accuracy of the database in terms of faithfulness. We present ready-to-use fitting formulas for equation of state-insensitive relations at merger (e.g. merger frequency), luminosity peak, and post-merger spectrum.

1. Introduction

The first observation of gravitational waves (GWs) from a binary neutron star (BNS) coalescence accompanied by electromagnetic (EM) signals marked a milestone in GW astronomy. Numerical relativity (NR) simulations are the main tool to explore the merger dynamics in the strong-field regime and aid the development of BNS gravitational waveforms that are necessary for GW detection and parameter estimation. The largest NR waveforms public catalogs contain data from thousands of binary black holes (BBHs) simulations, covering a significant portion of the mass-ratio and spin parameter space for quasi-circular mergers [1–7] and explore mergers from eccentric and generic orbits [4–6]. Public waveforms from simulations of binaries with NSs are more limited, and include the CoRe database [8] (164 binaries at different resolutions for a total of 367) and the SACRA-MPI [9, 10] (46, total 276), and SXS (2, total 6) [3, 11]. These waveforms are crucial for developing accurate inspiral-merger GW templates with tidal effects [12–24] and postmerger emission [25–36] with direct applications to equation of state (EOS) constraints [37–40]. The NR simulations performed for these waveforms are also key to determine the properties of the remnants from the binary parameters and the input physics (EOS, mass, spins, etc.), e.g. [25, 41–49] (see also [50, 51] for recent reviews). Consequently, new and extended data releases are necessary to support research in the field of GW astronomy.

Here, we present a new release of the CoRe database that comprises 90 new physically distinct BNS configurations at multiple resolutions, for a total of 254 binaries and 590 simulations. The new release includes GW strains and Weyl multipoles information up to the $(\ell, m) = (4, 4)$ mode. The new data were computed in simulations presented in Refs. [52–64] and include BNS waveforms consistent with the GW events GW170817 [54, 56, 57, 65] and GW190425 [64, 66].

The paper is organized as follows. Sec. 2 summarizes the employed simulation techniques. Sec. 3 describes the physics content of the database and the impact of the binary parameters on the waveforms. Sec. 4 presents a full merger waveform error analysis for a case study, and gives an overview of the average accuracy of the data. Sec. 5 presents, as a first application of the database, ready-to-use EOS-insensitive fitting formulas for the GW frequency, amplitude and the peak luminosity that characterize the merger as well as analogous relations for the post-merger GW spectra.

The CoRe database is hosted on the public `gitlab` server

`https://core-gitlfs.tpi.uni-jena.de/core_database`

Associated code repositories and resources can be accessed from

`http://www.computational-relativity.org/`

In particular, we provide the python package `watpy` to ease the checkout of the data and perform standard waveform analyses.

1.1. Notation

NR data are computed in geometrized units $c = G = 1$ and solar masses $\mathrm{M}_\odot$; we use these units also in this paper unless explicitly indicated. We recall that $GM_\odot/c^3 \simeq 4.925490947$ μs and $GM_\odot/c^2 \simeq 1.476625038$ km. The binary mass is $M = m_1 + m_2$, where $m_{1,2}$ are the gravitational masses of the two stars. The mass ratio is defined as $q = m_1/m_2 \geq 1$, and the symmetric mass ratio is $\nu = m_1 m_2/M^2 \in [0, 1/4]$, where $\nu = 1/4$ corresponds to the equal-mass case, whereas $\nu \to 0$ for very unequal masses. The dimensionless, mass-rescaled spin vectors are denoted with $\boldsymbol{\chi}_i$ for $i = 1, 2$ and the spin components aligned with the orbital angular momentum $\mathbf{L}$ are simply labeled as $\chi_i = \boldsymbol{\chi}_i \cdot \mathbf{L}/|\mathbf{L}|$. The effective spin parameter $\chi_{\rm eff}$ is defined as the mass-weighted aligned spin,

$$\chi_{\rm eff} = \frac{m_1\chi_1 + m_2\chi_2}{M}\,. \tag{1}$$

Similarly, one can define the spin parameter [67],

$$\hat{S} = \left(\frac{m_1}{M}\right)^2 \chi_1 + \left(\frac{m_2}{M}\right)^2 \chi_2. \tag{2}$$

The quadrupolar tidal polarizability parameters are defined as $\Lambda_i = (2/3)\, k_{2,i}\, C_i^{-5}$ for $i = 1, 2$ [68], where $k_{2,i}$ and C_i are respectively the $\ell = 2$ gravito-electric Love numbers and the compactness of the i-th neutron star (NS). The tidal coupling constant is [68]

$$\kappa_2^{\rm T} = 3\nu \left[\left(\frac{m_1}{M}\right)^3 \Lambda_1 + (1 \leftrightarrow 2)\right]\,, \tag{3}$$

that, similarly to the reduced tidal parameter [69]

$$\tilde{\Lambda} = \frac{16}{13}\frac{(m_1 + 12m_2)m_1^4\Lambda_1}{M^5} + (1 \leftrightarrow 2)\,, \tag{4}$$

parametrizes the leading-order tidal contribution to the binary interaction potential and waveform phase (note that $\kappa_2^{\rm T} = \frac{3}{16}\tilde{\Lambda}$ for $q = 1$.)

The radiated GW (polarizations h_+ and $h_\times$) is decomposed in (ℓ, m) multipoles as

$$h_+ - \mathrm{i}h_\times = D_L^{-1} \sum_{\ell=2}^{\infty} \sum_{m=-\ell}^{\ell} h_{\ell m}(t)\, {}_{-2}Y_{\ell m}(\iota, \varphi), \tag{5}$$

where D_L is the luminosity distance, ${}_{-2}Y_{\ell m}$ are the $s = -2$ spin-weighted spherical harmonics and ι, φ are respectively the polar and azimuthal angles that define the orientation of the binary with respect to the observer. Each mode $h_{\ell m}(t)$ can be decomposed in amplitude $A_{\ell m}(t)$ and phase $\phi_{\ell m}(t)$ as

$$h_{\ell m}(t) = A_{\ell m}(t)\, \mathrm{e}^{-\mathrm{i}\phi_{\ell m}(t)}\,, \tag{6}$$

with a related GW frequency

$$\omega_{\ell m}(t) = \frac{\mathrm{d}}{\mathrm{d}t}\phi_{\ell m}(t)\,. \tag{7}$$

A dimensionless frequency $\hat{\omega} = GM\omega$ relates to the frequency in Hz according to the formula

$$f = \frac{\omega}{2\pi} \simeq 32.3125\,\hat{\omega}\,\left(\frac{M_\odot}{M}\right)\,\mathrm{kHz}\,. \tag{8}$$

The GW strain modes are related to the Weyl Ψ_4 curvature modes $\psi_{\ell m}$ by

$$\ddot{h}_{\ell m} = \psi_{\ell m}\,. \tag{9}$$

CoRe simulations compute only $\psi_{\ell m}$. However, the above equation can be integrated to obtain the strain, either by using the fix-frequency integration method [70] or directly in the time-domain and performing a polynomial correction, e.g. [12, 71, 72]. Comparisons between analytical and NR data often use the Regge-Wheeler-Zerilli normalized multipolar waveforms,

$$h_{\ell m} = \sqrt{(\ell+2)(\ell+1)\ell(\ell-1)}\,\Psi_{\ell m}\,. \tag{10}$$

The radiated energy is obtained as [44]

$$\mathcal{E}_{\rm rad} = \frac{1}{16\pi}\sum_{\ell=2}^{\ell_{\rm max}}\sum_{m=-\ell}^{\ell}\int_0^t \mathrm{d}t' |D_L\dot{h}_{\ell m}(t')|^2\,, \tag{11}$$

whereas the angular momentum is computed as

$$\mathcal{J}_{\rm rad} = \frac{1}{16\pi}\sum_{\ell=2}^{\ell_{\rm max}}\sum_{m=-\ell}^{\ell}\int_0^t \mathrm{d}t' m\left[D_L^2 h_{\ell m}(t')\dot{h}^*_{\ell m}(t')\right]\,. \tag{12}$$

The data released are computed with $\ell_{\rm max} = 4$. The binary dynamics can be characterized by the binding energy and the orbital angular momentum, we therefore work with the binding energy per reduced mass, obtained by substracting the GW energy loss from the initial ADM mass, $E_b = [(M_{\rm ADM}(t=0) - \mathcal{E}_{\rm rad})/M - 1]\nu^{-1}$ and the dimensionless rescaled angular momentum $j = (\mathcal{J}_{\rm ADM}(t=0) - \mathcal{J}_{\rm rad})(M^2\nu)^{-1}$, see [44,73] for details. The GW luminosity peak is computed as

$$L_{\rm peak} = \max_t \frac{\mathrm{d}\mathcal{E}_{\rm rad}(t)}{\mathrm{d}t} \approx \max_t\left[\frac{1}{16\pi}\sum_{\ell=2}^{\ell_{\rm max}}\sum_{m=-\ell}^{\ell}\left|D_L\dot{h}_{\ell m}(t)\right|^2\right]\,. \tag{13}$$

The *moment of merger* is defined as the time of the peak of $A_{22}(t)$, and referred simply as "merger" when it cannot be confused with the coalescence/merger process. Waveforms are often shown in terms of the retarded time

$$u = t - r_*(r) = t - \left[r + r_S\ln\left(\frac{r}{r_S} - 1\right)\right]\,, \tag{14}$$

where r is the coordinate extraction radius in the simulations (assumed close to the isotropic Schwarzschild radius), r_* is the associated tortoise Schwarzschild coordinate, and $r_S = 2M$ is the Schwarzschild radius.

2. Methods

2.1. Initial data

Initial data for CoRe simulations are generated solving Einstein's constraint equations in the conformal thin sandwich (CTS) formalism [74] assuming a helical Killing vector and imposing hydrodynamical equilibrium for the NS's fluid [75, 76]. It is assumed that the fluid is either irrotational or in a quasi-equilibrium state with constant rotational velocity, which allows for consistent simulations of NS with spin [77, 78]. In the latter formalism, the rotational part w^a of the fluid's velocity is determined by an angular velocity parameter ω^i as

$$w_i = \epsilon_{ijk}\omega^j(x^k - x^k_*)\,, \tag{15}$$

where x^k_* are the coordinates of the NS center. Possible definitions of spin for a star in a binary are discussed in Refs. [44, 79, 80]. The spin parameters given in the CoRe database are defined to be those of single NSs in isolation with the same rest mass and the same ω^i as the BNS components [44, 79, 81]. To construct initial data with abritrary eccentricities, we use an extension of the helical symmetry condition that is based on approximate instantaneous first integrals of the Euler equations and a self-consistent iteration of the CTS equations [82]. This method also allows us to create low-eccentricity initial data in quasi-circular orbits using an iterative procedure that combines initial data and evolution codes [79] (see also [83–85].)

CoRe initial data are calculated using either `Lorene` [86–88] or `SGRID` [77–79, 81, 89, 90]. Both codes use multi-domain pseudospectral methods to solve the CTS equations and surface-fitting coordinates that minimize spurious stellar oscillations at the beginning of the evolutions and guarantee accurate determination of the initial binary global quantities. `Lorene` can construct irrotational binaries with either piecewise polytropic or tabulated EOS. In the latter case, they are often obtained as cold, β-equilibrated slices of finite-temperature, composition dependent EOS. `SGRID` can generate irrotational or spinning binaries with piecewise polytropic EOS and arbitrary (or reduced) eccentricity. In particular, `SGRID` can simulate BNS in which the individual stars rotate close to the breakup spin and have masses which are $\sim 98\%$ of the maximum supported NS mass allowed by the EOS [81]. Evolutions of initial data generated with `SGRID` and `Lorene` were compared in Ref. [44], where we found them to be in good agreement.

Initial data in quasi-circular orbits are characterized by the following global quantities of the 3+1 hypersurfaces: the total baryon mass M_b (a conserved quantity along the evolution); the total binary gravitational mass M, i.e., the sum of the two gravitational masses of the bodies in isolation; the initial orbital frequency $\Omega \simeq \omega_{22}/2$ and the corresponding ADM mass $M_{\rm ADM}$ and angular momentum $J_{\rm ADM}$.

2.2. Evolution codes

CoRe simulations evolve initial data using a free-evolution approach to 3+1 Einstein

field equations based on the hyperbolic conformal formulations BSSNOK [91–93] or Z4c [94–96]. The latter is used for all of the newly released data (Ref. [63] also uses BSSNOK). The (1+log)-lapse and gamma-driver shift conditions are used for the gauge sector. The general relativistic hydrodynamics is solved in first-order conservative form [97]. Wave extraction is typically performed on coordinate spheres at finite radius placed in the wave zone of the computational domain (typically $R \sim 500 - 1000$ $M_\odot$) and calculating the Weyl pseudoscalar Ψ_4, see e.g. [98] for details.

Simulations are performed with two independent mesh-based codes: `BAM` [98,99] and `THC` [100–102], both developed and maintained within our collaboration. These codes employ adaptive mesh refinement (AMR) techniques in which the domain consists of a hierarchy of nested Cartesian grids (refinement levels). The grid spacing of each refinement level in each direction is half the grid spacing of its surrounding coarser refinement level. Finite difference stencils are used for the spatial discretization of the metric variables (usually at fourth order accuracy), and high resolution shock-capturing methods for the hydrodynamics. The Berger-Oliger or Berger-Colella algorithm is employed during the explicit mesh evolution. The latter is performed with the method of lines and Runge-Kutta schemes of third or fourth order accuracy in time. The innermost levels move dynamically during the time evolution following the motion of the NS such that the strong field region around a NS is always covered with the highest resolution. Both codes employ a hybrid OpenMP/MPI parallelization strategy and show good parallel scaling up to thousands of cores.

`BAM` implements high-order finite-differencing WENO schemes [17] and, more recently, an entropy-flux-limited (EFL) scheme [63], that is better adapted to the treatment of the NS surface, to accurately simulate multiple orbits and GWs from inspiral-mergers. The typical grid configurations for these simulations consist of seven refinement levels, where the innermost level split into two boxes covering each of the NS. Standard grids parameters for resolution studies are chosen with $n_m \in [96, 256]$ points per direction in each inner (moving) level and $n \in [144, 512]$ for the outer levels. The minimal grid spacing in each direction is $\Delta \sim [0.059, 0.321]$ $M_\odot$ and the maximal resolution reached in the released simulation is $\Delta \sim 0.06$ $M_\odot$. Symmetries can be imposed to reduce the computational cost of certain problems. For example, aligned-spin BNS are often simulated in bitant symmetry ($z > 0$ volume). The simulation parameters can vary for each simulation; the relevant ones are reported in the CoRe metadata.

`THC` implements both high-order finite-differencing schemes [103] and Kurganov-Tadmor-type central schemes. The latter are preferentially used with simulations with microphysics. `THC` can make use of microphysical EOS, and implements various neutrino transport schemes [52, 104, 105] (see below) and subgrid-scale treatment of turbulent mixing and dissipation (GRLES) [59,106] to accurately simulate remnants and postmerger dynamics. Most of the GRLES data in the current release employ an effective model for turbulence based on the high-resolution magnetohydrodynamics simulation of Ref. [107], where the viscosity parameter is set to $\nu_T = \ell_{\rm mix} c_s^2$ and c_s is the sound speed of the fluid. $\ell_{\rm mix}$ is typically defined to be a function of the rest-mass density calibrated

with the general-relativistic magneto-hydrodynamics simulations of [107] (see [59]). `THC` builds on the `Cactus` framework [108] and the `Einstein Toolkit` [109, 110]. `THC` simulations use the `Carpet` adaptive mesh refinement driver for `Cactus` [111], which implements both vertex centered and cell-centered adaptive mesh refinement with flux correction [112, 113]. The grid structure used in the `THC` simulations is similar to that used in `BAM`. The grid structure is specified by the resolution at the coarsest refinement level and at the location of the center of the neutron stars. The refinement levels on the grid hierarchy do not have to be connected and `Carpet` can merge different regions to create grids with complex topology. The standard resolution setup of the `THC` simulations uses a resolution of $\Delta = 0.125\ M_\odot$ in every direction on the finest refinement level. The maximal resolution reached in the released simulation is $\Delta \simeq 0.08\ M_\odot$. The typical CFL is 0.125. However, an even lower CFL of 0.0625 is used on the coarsest grid to handle the gamma-driver source term in the shift evolution equation. All `THC` simulations included in the current release of the CoRe database use bitant symmetry.

2.3. EOS models

CoRe simulations currently employ 18 different EOS models for the neutron star matter. `BAM` data are computed using analytical EOS in the form

$$P(\rho, \epsilon) = P_{\rm pwp}(\rho) + (\gamma_{\rm th} - 1)\rho(\epsilon - \epsilon_{\rm pwp})\,, \tag{16}$$

where $P_{\rm pwp}(\rho)$ is a given piecewise politropic EOS model [114]. It prescribes also a value $\epsilon_{\rm pwp}$ for the specific internal energy given the rest mass density ρ, augmented with a γ-law "thermal" pressure term (usually, $\gamma_{\rm th} = 1.75$). The specific parameters we employ for the piecewise polytropic EOS mimic well-established zero-temperature EOS models [114]; tables of these parameters are available on the CoRe website ‡.

The current release significantly extends the data computed with finite-temperature EOS over the first release. The release includes data from seven finite-temperature EOS, used in the calculation of Refs. [52–57, 61, 64]. The finite-temperature EOS include the following models: BHB$\Lambda\phi$ [115], BLh [116, 117], BLQ [61, 117], DD2 [118, 119], LS220 [120], SFHo [121], SLy4/SRO [122, 123].

All these EOS include neutrons, protons, nuclei, electrons, positrons, and photons as relevant thermodynamics degrees of freedom. The ALF2 [124] and BLQ EOS [61,117] are hybrid model accounting for deconfined quark matter. BHB$\Lambda\phi$ is a hadronic model that includes Λ hyperons [115, 125].

Cold, neutrino-less β-equilibrated matter described by these microphysical EOS predicts NS maximum masses and radii within a larger range than that allowed by current astrophysical constraints, including GW170817 [38, 39, 126]. Figure 1 shows the mass-radius diagram and the quadrupolar tidal polarizability parameter-mass diagram of these EOS. The largest radius of a $M = 1.4$ M$_\odot$ NS is $R_{1.4}^{\rm TOV} \sim 15.21$ km (EOS 2H) and the smallest radius ∼9.75 km (EOB 2B). The smallest maximum mass is $M_{\rm max}^{\rm TOV} \sim 1.70$ M$_\odot$ (EOS H3), whereas the largest is $M_{\rm max}^{\rm TOV} \sim 2.83$ M$_\odot$ (EOS 2H).

‡ `http://www.computational-relativity.org/eos/`

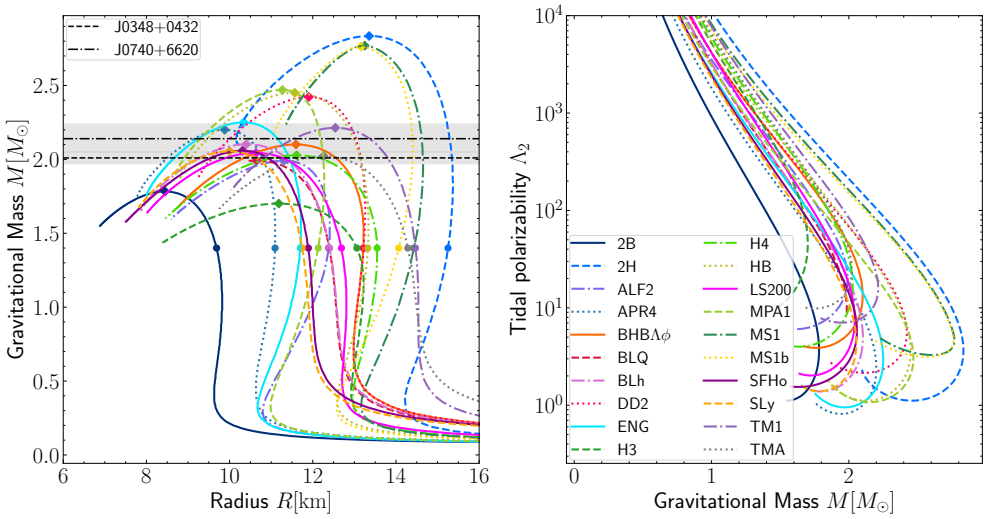

Figure 1. Mass-radius (left) and tidal polarizability-compactness (right) sequences of the available EOS. Diamond-shaped markers correspond to the maximum mass for each EOS, whereas the circle-shaped ones show the radius $R_{1.4}$ for a 1.4 $M_\odot$ star.

Most of these EOS can be found on the CoRe website in tabulated form. In the simulations, the EOS is called during the hydrodynamics evolution in order to compute the pressure from the rest-mass density, the temperature, and the electron fraction, i.e., in the form $p = P(\rho, T, Y_e)$. Any relevant thermodynamical quantity is evaluated by multi-linear interpolating the tabulated values in $\log \rho$, $\log T$, and Y_e. As common in relativistic hydrodynamics, the EOS is called during the transformation from conservative to primitive variables. The latter takes place at each timestep and grid point and it involves a numerical root finding of the function $f(p) := p - P(\rho, \epsilon, Y_e)$, where the specific internal energy ϵ is implicitly given by the temperature T [127]. Hence, each root-finding step includes another root finder for the function $g(T) = \epsilon - \mathcal{E}(T)$ (see [128] for a discussion on computational efficiency and a non-standard approach based on neural networks.)

2.4. Microphysics

Most of the `THC` simulations account for the loss of energy and lepton number due to the net emission of neutrinos using a leakage scheme [104, 127]. Accordingly, effective neutrino leakage rates are computed as a physically motivated interpolation from the emission and diffusion rates. The latter require the knowledge of the optical depth of each computational zone in such a way as to recover the correct cooling time scale. Neutrino reabsorption is included in some simulations using the M0 scheme [104]. This scheme splits neutrinos in an optically thick component, treated with the leakage scheme, and a free-streaming component. The free-streaming neutrinos and their average energies are obtained by solving the radiative transfer equations on a set of

Table 1. Weak reaction rates and references for their implementation. We use the following notation $\nu \in \{\nu_e, \bar{\nu}_e, \nu_x\}$ denotes a neutrino, ν_x denote any heavy-lepton neutrino, $N \in \{n, p\}$ denotes a nucleon, and A denotes a nucleus.

Reaction	Reference
$\nu_e + n \leftrightarrow p + e^-$	[129]
$\bar{\nu}_e + p \leftrightarrow n + e^+$	[129]
$e^+ + e^- \rightarrow \nu + \bar{\nu}$	[130]
$\gamma + \gamma \rightarrow \nu + \bar{\nu}$	[130]
$N + N \rightarrow \nu + \bar{\nu} + N + N$	[131]
$\nu + N \rightarrow \nu + N$	[130]
$\nu + A \rightarrow \nu + A$	[132]

radial rays (the so-called ray-by-ray approach) fully-implicitly in time. More recently, we have implemented an energy-integrated M1 scheme in `THC` [105]. The new scheme can self-consistently capture the diffusion of neutrinos from the merger remnant and its reabsorption in the ejecta. M1 simulations are not included in the current release of the database, but will be made public as soon as the associated publications have been accepted. Table 1 summarizes all neutrino reactions currently included in `THC` together with the reference in which the form of the rates we use are derived.

3. Overview

CoRe simulations are performed for various binary masses, mass ratios, NS spins and EOS as summarized by Figure 2. They cover a significant portion of the BNS parameter space and allow to quantitatively explore the connection between the gravitational-wave morphology and the binary parameters in some detail. Figure 3 illustrates the variety of waveforms contained in the database. In the following, we give an overview of the database content and outline the connections between physics and waveform morphology.

The database contains waveforms from binaries with total masses ranging from 2.4 $M_\odot$ to around $\sim$3.4 $M_\odot$ with 45 datasets reaching mass ratios larger than $q \gtrsim 1.4$ and up to $q = 2.1$ [45, 56, 62]. EOS effect can be summarized to some extent § by the quadrupolar tidal polarizability parameters $\Lambda_{1,2}$ [68], where larger (smaller) values of Λ_i are associated to stiffer (softer) EOSs. The most compact NSs (and most massive binaries) are associated with the smallest values of $\Lambda_{1,2}$ (and $\tilde{\Lambda}$), see the right panel of Fig. 1. The CoRe data encompasses well the mass and EOS variation for realistic BNSs. Waveforms from both irrotational and spinning (using the formalism outlined in Sec. 2.1) quasi-circular mergers are included [44, 46, 58]. For aligned spins, the

§ A NS spacetime is characterized by an infinite number of multipolar Love number of gravitoeletric and gravimagnetic type; Λ_2 parametrizes only the (gravitoelectric) leading order term in the Lagrangian.

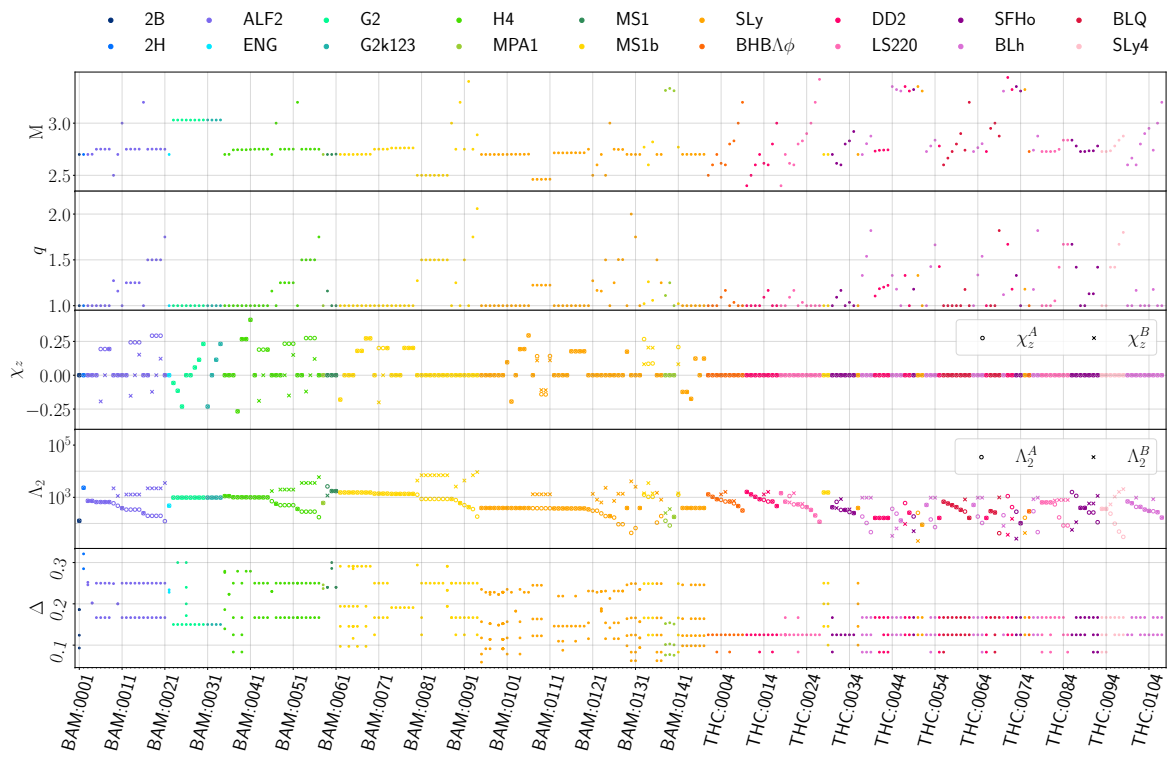

Figure 2. Summary of the CoRe database. The complete data are shown based on: the binary mass M, the mass ratio q, the individual dimensionless spins $\chi_z^{\rm A,B}$, the individual quadrupolar tidal parameters $\Lambda_2^{\rm A,B}$, the EOS and the employed resolution Δ.

individual dimensionless components range in $\chi_z \in [-0.25, 0.5)$; about 7 datasets are from simulations with precession effects [46, 58]. The distribution of key parameters among the CoRe simulations is shown in Fig. 4.

Most of the CoRe waveforms are produced from quasi-circular mergers. The residual eccentricities of non-iterated quasi-circular initial data is usually $e \sim 10^{-2} - 10^{-1}$, see the bottom right panel of Fig. 4. About 13 datasets have an initial eccentricity $e \lesssim 10^{-3}$ that was reduced through an iterative procedure employing the formalism described in Sec. 2.1. A subset of waveforms refer instead to eccentric mergers with initial eccentricity values as high as $\sim$0.7 [104, 133, 134]. In particular, the simulation in the bottom panels of Fig. 3 has an initial eccentricity of 0.55.

The effects of mass-ratio, spin, and tides on the orbital dynamics can be studied by means of gauge-invariant energy curves $E_b(j)$, that are also publicly released. We illustrate this in Fig. 5 for a few examples. In the inspiral, the binary's angular momentum j decreases due to GW emission and the system becomes more bound (E_b stays negative and $|E_b|$ increases). Equal mass ($\nu = 1/4$) non-spinning BBH systems merge with $E_b \simeq -0.12$, indicating that about 3% of the binary mass was radiated in GWs to the moment of merger (marker in the figure). Tidal effects in BNS make the

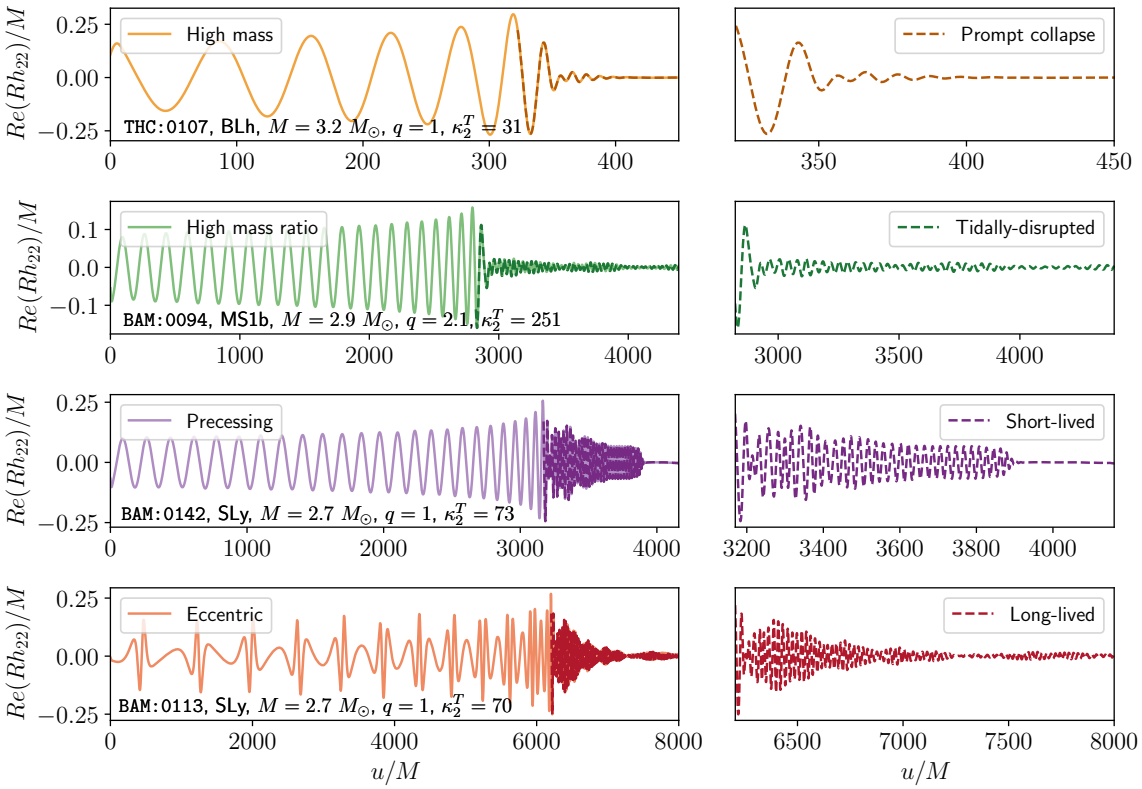

Figure 3. Representative waveforms from the CoRe database with their respective post-merger signals exemplifying the different morphologies influenced by the input physics (total mass of the binary, mass ratio, spins, and eccentricity).

potential governing the relative dynamics more attractive. The tidal constribution to the potential at leading order is $\sim -\kappa_2^{\rm T}/r^6$, i.e. it is stronger for larger tidal polarizabilities $\Lambda_{1,2}$ and it is short-ranged thus affecting the motion mostly at high frequencies (small separations, r) towards merger. Consequently, the inspiral of an equal mass non-spinning BNS is faster than a binary black hole inspiral. The binding energy at the moment of merger is $|E_b| \sim 0.064$, which is smaller than the black hole case because the BNS system is less compact. Mass-ratio effects make the potential more repulsive, but are less effective than tides at high frequencies. The $q = 2$ BNS shown in Fig. 5 merges at smaller values $|E_b| \sim 0.055$ than the equal mass because of tidal disruption. The remnant has also larger angular momentum $j \sim 3.6$ [57].

Spin-effects are dominated by the leading-order spin-orbit interaction; their character is thus repulsive or attractive depending on the projection of the spin on the orbital angular momentum [135]. This is analogous to what happens to corotating/counter-rotating circular orbits in Kerr spacetimes that move outwards (inwards) for antialigned (aligned) spin configurations with respect to the nonspinning case. In binary black hole simulations this effect has been named as "hang-up" effect [136]. In Fig. 5, the spinning BNS with $\hat{S} = 0.1$ is more bound than the non-spinning BNS at the moment of merger with $E_b \sim -0.068$. Note that j in this case includes the

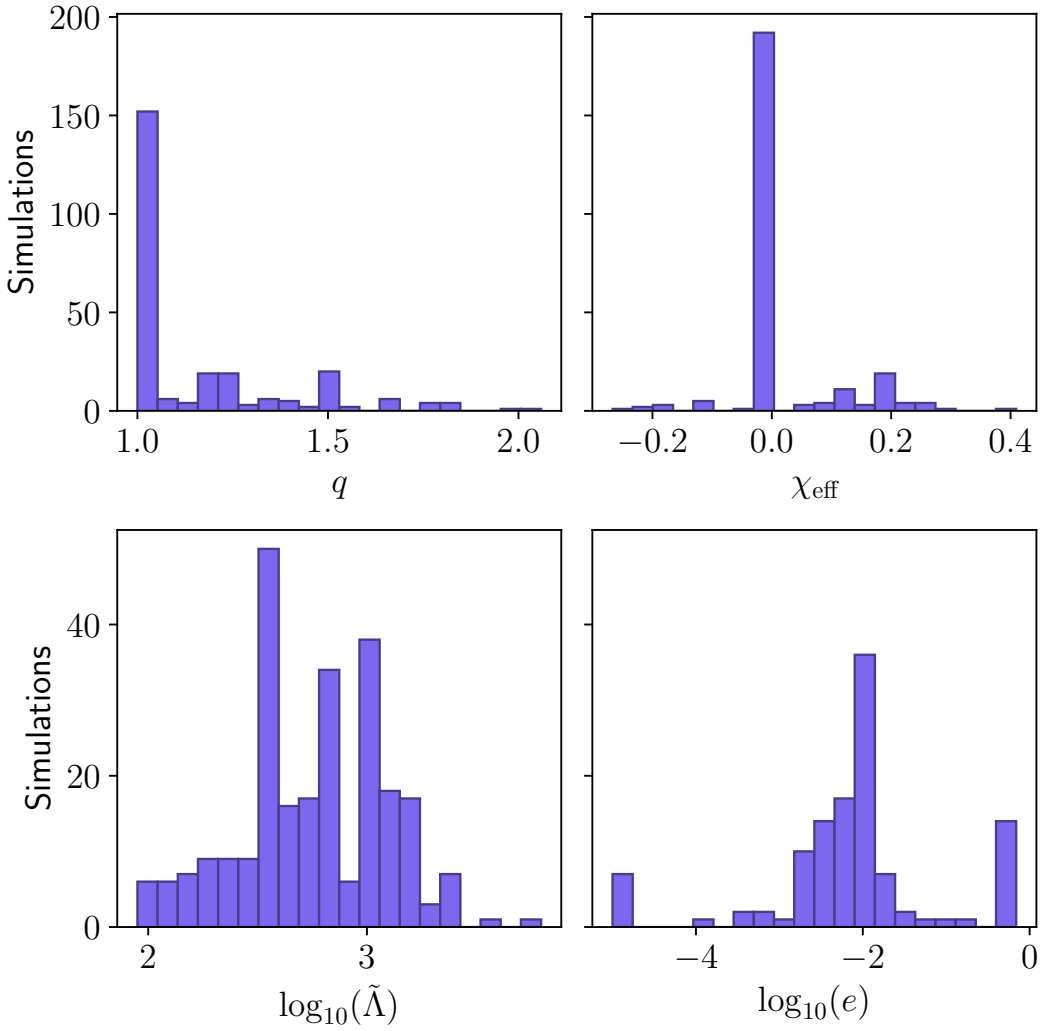

Figure 4. Distribution of the mass ratio q, and the effective spin parameter $\chi_{\rm eff}$, reduced tidal parameters $\tilde{\Lambda}$, and initial eccentricity of the 254 CoRe database configurations. Note that for some short simulations no reliable measure of eccentricity was possible.

spin contribution. Moreover, the eccentric equal-mass case, contrary to the previous ones, shows brief moments of constant E_b indicating the times when the NSs are apart (see inset of Fig. 5). Energy curves for BNS have been studied in detail in [44, 46, 58] to which we refer for more details. We stress that the properties of BNS systems at the moment of merger can be captured by EOS-insensitive (quasi-universal) relations [14]. The latter can be helpful in waveform modelling and used to estimate the properties of the remnant. We refer to Sec. 5 for further discussion.

High-mass BNS produce a remnant that promptly collapses to a black hole shortly

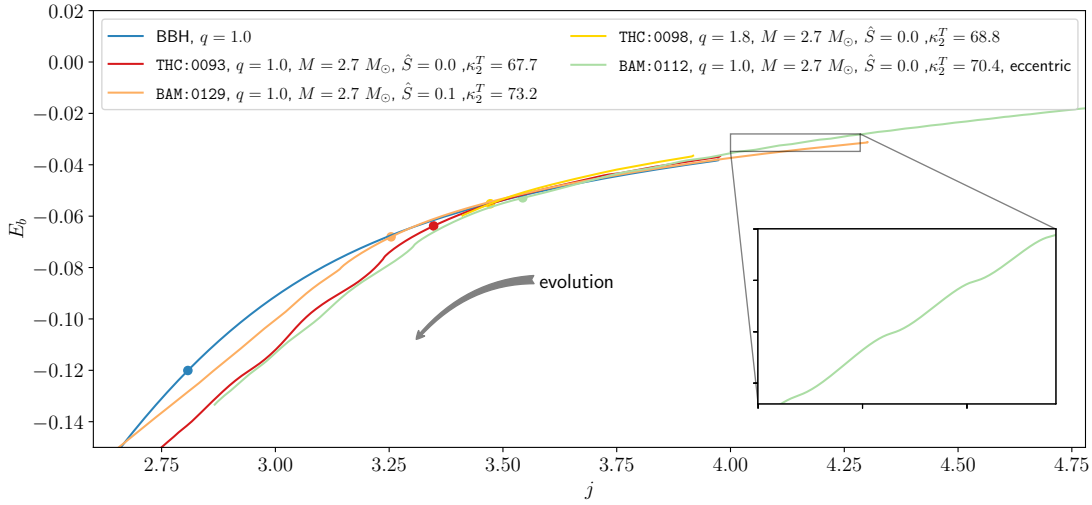

Figure 5. Energy curves $E_b(j)$ for selected binaries. The binary's binnding energy and angular momentum evolve in time from right to left along the cuves $E_b(j)$. The moment of mergers are indicated with a marker. The close up of `BAM:0112` shows a modulation present due to its eccentric inspiral (see text).

after the moment of merger and before the two cores can bounce [50,51]. Prompt collapse implies negligible shocked dynamical ejecta, because the bulk of the mass ejection comes from the first core bounce after their collision [52]. Prompt collapse can be characterized by a threshold mass $m_{\rm thr} = k_{\rm thr} M_{\rm max}^{\rm TOV}$, that mainly depends on the maximum mass of cold equilibria $M_{\rm max}^{\rm TOV}$ supported by the EOS [43, 137]. The recent analysis of Ref. [138], based on 227 finite-temperature EOS and CoRe data ‖, found that the prompt collapse mass threshold for equal-mass non-spinning BNS is well described by an EOS-insensitive threshold

$$k_{\rm thr} = a\, C_{\rm max}^{\rm TOV} + b\,, \tag{17}$$

where $C_{\rm max}^{\rm TOV}$ is the compactness of the maximum NS mass, and $a = -3.36 \pm 0.20$, $b = 2.35 \pm 0.06$. A prompt collapse waveform has a rapidly damped black hole ringdown after the moment of merger as shown in the top panels of Figure 3. Consequently, the postmerger GW signal is practically negligible for the sensitivities of both current and next-generation detectors. The lack of shocked ejecta and of a massive disc also implies that equal-mass prompt-collapse mergers have dim EM emission. However, for very asymmetric BNS with $q \gtrsim 1.4$, it is the tidal disruption of the secondary NS and its accretion onto the primary to trigger the gravitational collapse [56]. Thus, asymmetric mergers can be electromagnetically bright because they produce massive tidal dynamical ejecta and remnants with accretion discs of mass $\sim$0.1 $M_\odot$. This prompt collapse process is mainly controlled by the incompressibility parameter of nuclear matter around the TOV maximum density [139]. A robust, EOS-insensitive criterion is not known in these

‖ These data are not released in the database since the waveforms are rather short and extracted at close radii.

conditions [56,139–142], but tidal disruption effects are subdominant to the mass effect; they produce maximal variations from the equal-mass criterion of ∼8% [138,139].

Without prompt collapse, the evolution of a NS remnant is driven by the GWs emission of $\sim 10^{53}$ erg lasting $\lesssim$20 milliseconds (GW-driven phase) [143,144]. During this phase, a remnant that collapses to black hole is called *short-lived*, while a remnant that settles to an approximately axisymmetric rotating NS is called *long-lived*. Examples of postmerger signals from these remnants are shown in the last two panels on the right of Figure 3, for the equal-mass case. The GW-driven phase is associated to a luminous GW transient that peaks at frequencies $\sim 2-4\,\mathrm{kHz}$ [25,26,145–148]. The spectrum of this transient is rather complex but has robust and well-studied features at a few characteristic frequencies. Most of the GW power is emitted in the $(2,2)$ mode at a nearly constant frequency $\omega_{22}(t) \approx 2\pi f_2$; the more compact and close to collapse the remnant is, the higher and more varying the $\omega_{22}(t)$ emission frequency is. The postmerger dynamics is primarily controlled by the masses of the two stars and the bulk properties of the zero-temperature EOS, in particular maximum TOV mass and compactness [50,149]. Finite temperature and neutrinos do not produce qualitative differences, other than possibly on the time of gravitational collapse of the remnant [150]. Quantitative differences in the GW signal introduced by finite-temperature and neutrino effects are typically subdominant compared to finite-resolution uncertainties [105,151]. On the other hand, microphysics plays a crucial role in the EM counterparts and nucleosynthesis from mergers, e.g., [104,152–155].

The remnant's signal from asymmetric binaries with mass ratio $q \gtrsim 1.4$ carries the imprint of the tidal disruption during merger [45,56,156]. An example of such a waveform is shown in the second panels (top to bottom) of Figure 3. Comparing to the equal-mass long-lived case, the postmerger amplitude is significantly smaller because the asymmetric remnant does not experience the violent bounces of the symmetric remnant. For the same reason, the early-times modulations in frequency and amplitude present in the equal-mass case are significantly suppressed in the asymmetric case.

The evolution of a NS remnant beyond the GW-driven phase is uncertain at present. Explorations of the viscous phase using NR simulations have started [57,157,158], but they are still incomplete in many ways. While GWs emission is expected significantly weaker than during merger, remnant's instabilities might enhance GW emission. Current NR results suggest that BNS remnants have an excess of both gravitational mass and angular momentum after the GW-driven phase and when compared to equilibrium configuration with the corresponding baryon mass [159]. Possible mechanisms to shed (part of) this energy are CFS [160,161] and one-arm instabilities [162,163] that would lead to potentially detectable, long GW transients at $\lesssim$1 kHz. Example of such waveforms are `THC:0028`, `THC:0029`, and `THC:0036` [163].

Finally, CoRe data are available for multiple grid resolutions as discussed in Sec. 2 and shown by Fig. 2. Most of the newly released data contain high resolution simulations with a minimum grid spacing as low as $\Delta \sim 0.06\ \mathrm{M}_\odot$, e.g., the NS are resolved with a uniform mesh of spacing ∼884 meters. Notably, simulations of more than 20 orbits or

up to hundreds milliseconds postmerger and with microphysics were performed at these resolutions. Simulations at multiple resolutions are a crucial aspect for data quality that is discussed next.

4. Waveform accuracy

Waveform accuracy depends on several aspects of the simulations. Within the CoRe data the largest sources of uncertainty are (i) the truncation error of the numerical scheme, that is regulated by the mesh resolution employed in the simulations, and (ii) the finite extraction radius for the GW data, e.g. [17, 63, 101, 164]. Other aspects are relevant for waveform modelling, as for example, the length of the simulation (number of orbits/GW cycles), the residual eccentricity in quasi-circular initial data, and the simulation of realistic physics (star rotation, EOS, etc.).

Waveform accuracy should be studied by the user case-by-case considering amplitude and phase plots with datasets of simulations at different resolutions and extraction radii. This analysis typically requires a minimum of three simulations of the same BNS at different grid resolutions (a "convergent series") and has been performed by few authors, including members of the CoRe collaboration [9,10,17,63,101–103,164]. We give below in Sec. 4.1 a complete example of error analysis of a ∼10 orbit inspiral-merger waveform.

In GW astronomy, the quality of a waveform template is commonly assessed using the Wiener product (*overlap*) between two waveforms $h_{1,2}(t)$ for a given detector [165],

$$\langle h_1, h_2 \rangle := 4\Re \int \frac{\tilde{h}_1(f)\tilde{h}_2^*(f)}{S_n(f)} df \,, \tag{18}$$

where $S_n(f)$ is the power spectral density (PSD) of the detector noise and $\tilde{h}_{1,2}(f)$ the Fourier transform of $h_{1,2}(t)$. The inner product allows to define "accuracy standards" for either detectability or measurements (parameter estimation), e.g., Ref. [166–172]. In the former case, one is interested in quantifying the fractional loss of signal-to-noise ratio (SNR) due the use of a sub-optimal, discrete match filter. Since the number of GW events is proportional to the observable volume, and the distance is inversely proportional to the observed SNR, the fractional loss of potential events scales like the cube of the minimum overlap in the discrete template bank [166,167,172]. In the latter case, one is interested in quantifying the bias (or the maximum knowledge) on the GW parameters given the noise in the detector (statistical errors) [168,169,172]. In practice, one proceeds by defining the *faithfulness* between two waveforms

$$\mathcal{F} := 1 - \max_{t_0,\phi_0} \frac{\langle h_1, h_2 \rangle}{\|h_1\| \|h_2\|}, \tag{19}$$

where t_0 and ϕ_0 are a reference initial time and phase, and its complementary, the unfaithfulness, $\bar{\mathcal{F}} := 1 - \mathcal{F}$. By demanding that, at worst, the systematics biases become of the same order as the statistical ones when the noise level is doubled, it is

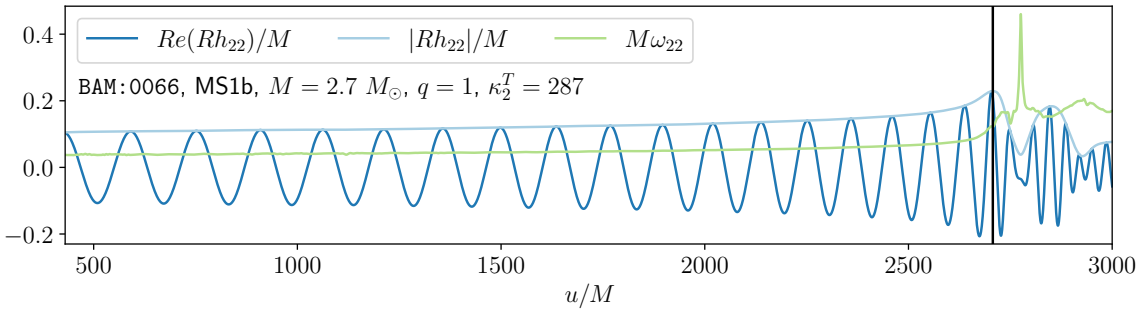

Figure 6. The real part of the strain Rh_{22}, its amplitude $|Rh_{22}|$, and frequency $M\omega_{22}$ of `BAM:0066`. The black solid line indicates the moment of merger.

possible to establish the condition [172]

$$\mathcal{F} > 1 - \frac{\epsilon^2}{2\rho^2}\,, \tag{20}$$

where ρ is the SNR and $\epsilon^2 \ll 1$. This condition is *necessary* for unbiased parameter estimation (faithful waveforms); its violation does not imply that an analysis has biases [164, 169, 173, 174]. The above criterion can be used to quantify the accuracy of NR data, for example by calculating the faithfulness between data at different resolutions [63, 164, 174]. We will use the faithfulness measure in Sec. 4.2 to discuss the average accuracy of the data of the CoRe database.

4.1. Example of NR waveform analysis

In this section we present a waveform error analysis for `BAM:0066` [18]. The strain Rh_{22} at the lowest extraction radius available for this simulation, $R = 700\,\mathrm{M}_\odot$, its amplitude $|Rh_{22}|$ and frequency $M\omega_{22}$ are shown in Figure 6. Note that in this section we use R instead of D_L.

In order to test self-convergence, we compare amplitude and phase differences of $R\psi_{22}$ between the different resolutions. For this case, we consider the simulation at resolutions $n_m = 120, 160, 240$ grid points on the highest refined AMR level; hereafter Low (L), Medium (M), and High (H). The convergence rate p is found experimentally by rescaling these differences using the scaling factor SF [164],

$$\mathrm{SF} = \frac{\Delta_\mathrm{L}^p - \Delta_\mathrm{M}^p}{\Delta_\mathrm{M}^p - \Delta_\mathrm{H}^p} \tag{21}$$

where Δ_x is the grid spacing at resolution x. We show the self-convergence test in Figure 7. The differences decrease with increasing resolution, as one would expect from convergent data. They also increase with increasing simulation time because truncation errors accumulate during the simulation. The optimal scaling is found for $p = 2$ with $\mathrm{SF}(2) = 1.4$, thus indicating second order convergence. In presence of convergence, a measure of the error to be assigned to the (highest resolution) data is given simply by the difference between the two highest resolutions. This is a conservative estimate

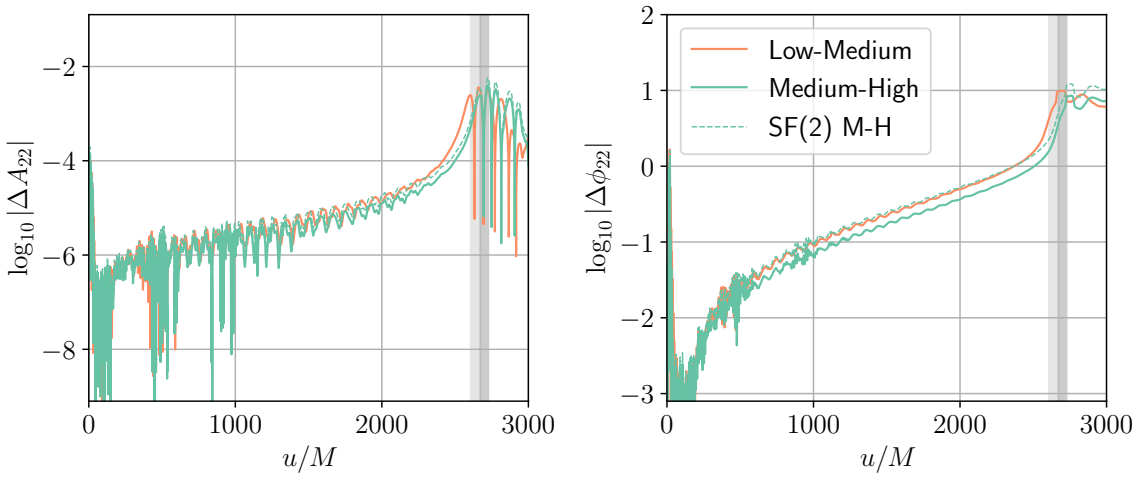

Figure 7. Self-convergence tests of `BAM:0066` $R\psi_{22}$ The dashed blue line represents the rescaled difference for second order convergence. The light (dark) gray shaded regions show the time of merger differences of Low-Medium (Medium-High) resolutions.

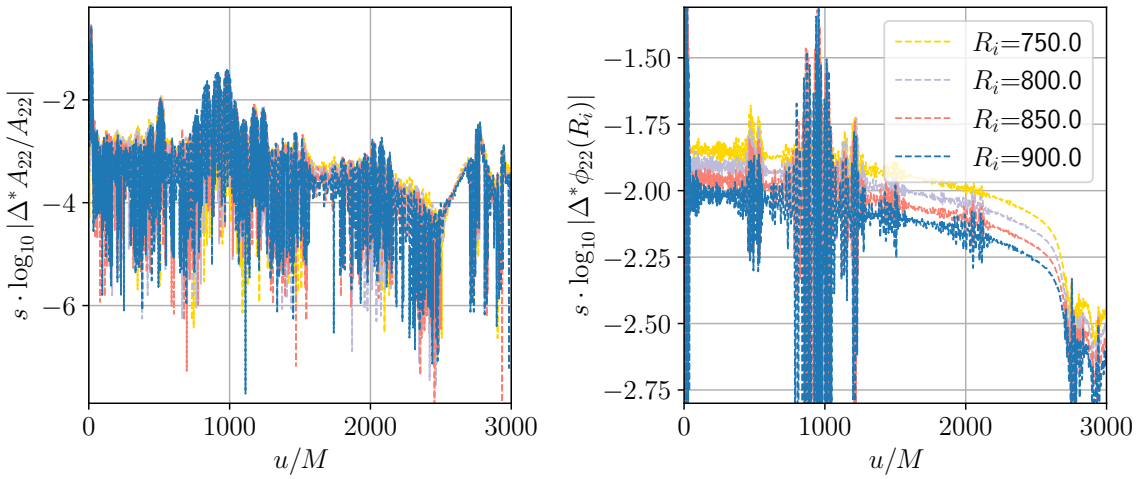

Figure 8. Amplitude (left) and phase (right) differences between `BAM:0066`'s $R\psi_{22}$ extracted at consecutive finite-radii $R_i = 700, 750, 800, 850, 900$ $M_\odot$.

because (for convergent data) the truncation error is certainly smaller. Alternatively, the experimental convergence factor can be in principle used in a Richardson extrapolation of the data to provide an improved dataset and error estimate [17, 164]. Note that in this procedure the waveforms are not shifted by a relative time and phase shift because the simulations of the convergent series are run using the same initial data with a fixed initial phase.

To assess the uncertainties originated from the waveform obtained at finite-extraction radii, R_i, we compare the phase differences between consecutive radii [164]

$$\Delta^*\phi_{22}(R_i) = \phi_{22}(R_i) - \phi_{22}(R_{i-1})\,, \tag{22}$$

and similarly for the relative amplitudes, $\Delta^* A_{22}/A_{22}$. In Fig. 8 we show the differences at the extraction radii $R = 700, 750, 800, 850, 900$ $M_\odot$. The phase differences decrease at progressively large radii, thus indicating the numerical waveforms are converging towards their true morphology at null infinity. The phase differences are larger at early times and decrease towards merger; note this behaviour has the opposite sign of that of resolution effects [17]. The relative differences in amplitude are $\sim 10^{-4}$ for all radii, indicating robust results are obtained already with relatively close extraction sphere. The waveforms can be extrapolated to null infinity using either a polynomial in $1/R$ of order K [164] or the method outline in [175]. The two methods give comparable results; the former is more general and can be applied to the curvature multipoles $\psi_{\ell m}$, the latter is a simpler method for the strain modes. An error due to finite extraction can be then assigned to the data at finite extraction as the difference with the extrapolated data (or viceversa). Another method is to post-process simulations using Cauchy characteristic extraction (CCE) [176] and simulate waveform at future null infinity. This technique was used for some of the CoRe data.

The total error budget can be computed as the sum in quadrature of the truncation and finite extraction errors, and it is shown in Fig. 9 for both the curvature and strain (2,2) modes. As mentioned above, the truncation phase error is typically a factor ~ 2 larger than the finite extraction error (for $R \gtrsim 500 M_\odot$) at merger and in simulations with tens of orbits.

Finally, we obtain the unfaithfulness $\bar{\mathcal{F}}$ of the waveforms between the different resolutions (M-H and L-M). The Wiener integral is evaluated in the frequency range $f \in [f_{\rm min}, f_{\rm mrg}]$ and employing the Advanced LIGO PSD P1200087 [177] from `bajes` [178]. Here $f_{\rm min}$ corresponds to the initial GW frequency, and $f_{\rm mrg}$ to the frequency at the moment of merger. For the faithfulness threshold $\mathcal{F}_{\rm thr}$ in Eq. (20), we consider $\epsilon^2 = 1$ as the strict requirement, and $\epsilon^2 = 6$, corresponding to the number of intrinsic parameters of a BNS. Similarly to [63], the SNR values are chosen to be $\rho = 14, 30, 80$. Figure 10 shows the computed values. The smallest unfaithfulness (M-H, $n_m = 240, 160$) passes five out of the six accuracy tests, whereas the other one (L-M, $n_m = 160, 120$) passes only two, namely $\mathcal{F}^{14,6}_{\rm thr}$ and $\mathcal{F}^{30,6}_{\rm thr}$. However, the unfaithfulness value lies closely (or on top) of the threshold $\mathcal{F}^{14,1}_{\rm thr}$.

Analyses similar to the one above are necessary to determine the quality of the NR data for GW modelling. Convergence of the data is a necessary requisite for robust error estimates. Other diagnostic quantities used to verify convergence in simulations are constraint violation, baryon mass conservation and the stars oscillations during the first orbits, e.g. [58, 79, 96, 99, 164]. Achieving waveform convergence in long-term evolutions of BNS is a nontrivial result and, in our experience, requires at least fifth order finite-differencing schemes or finite volume schemes with fifth order reconstructions (at the current resolutions) [17, 63, 102]. Second [17], approximately third [102] and clear fourth order convergence [63] has been demonstrated up to merger in some data using these finite-differencing conservative schemes. Extreme mass ratios $q \sim 2$ and NS rotation close to the breakup limit remain challenging to simulate as well as to obtain clean

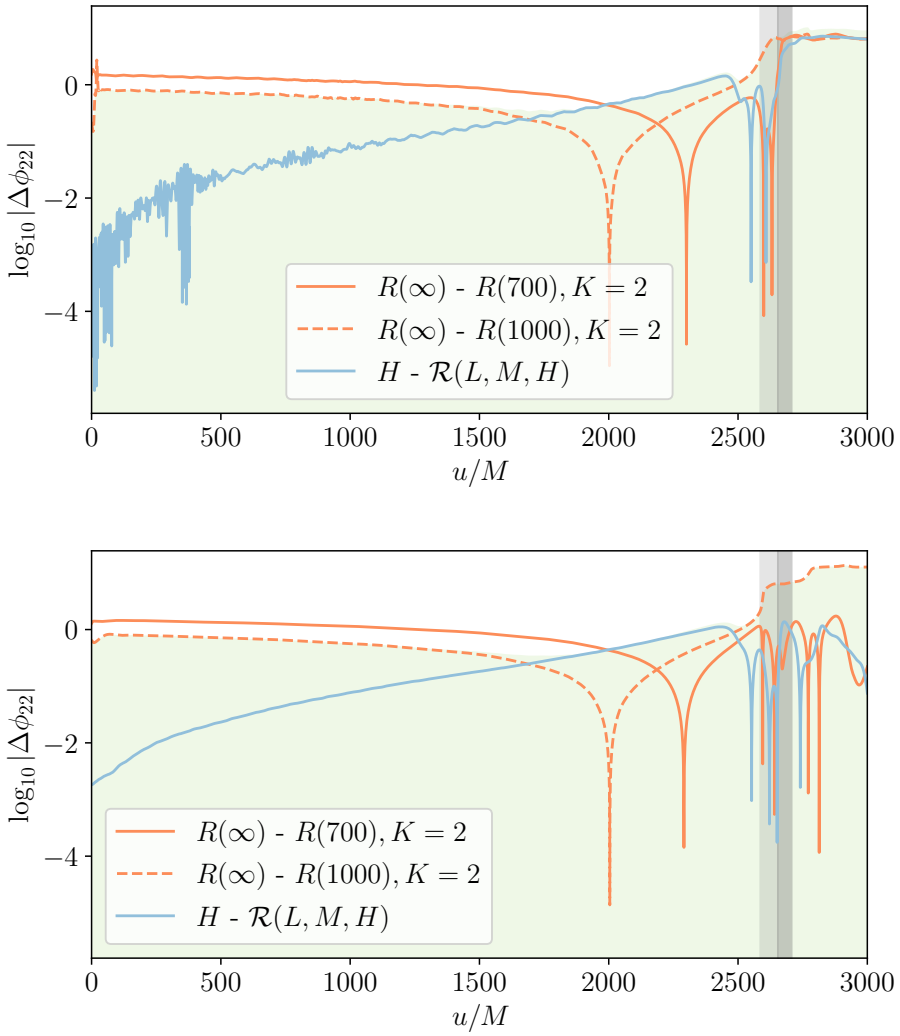

Figure 9. Error budget (shown as a green shaded area) for the phase of $R\psi_{22}^4$ (top) and Rh_{22} (bottom) from the truncation error (blue line) and finite-radius extraction uncertainty (orange lines) employing polynomial extrapolation with $K = 2$. The blue line shows the difference between the highest resolution and the Richardson extrapolated dataset $\mathcal{R}(L, M, H)$.

convergence in GW higher (subdominant) modes like $(\ell, m) = (2, 1), (3, 3)$ and $(4, 4)$. Work in these directions is ongoing [56, 60, 62, 63]. For example, clear fourth order convergence in the subdominant (3, 2) and (4, 4) modes for $q = 1$ has been shown in [63]. Postmerger waveforms typically show slower convergence due to shock formation at merger and the complex fluid dynamics in the remnant. Nonetheless, GW spectra have remarkably robust features that can be accurately quantified with NR data, as we shall discuss in Sec. 5. We refer the reader to Ref. [31, 36] for recent work on the accuracy of CoRe postmerger waveform.

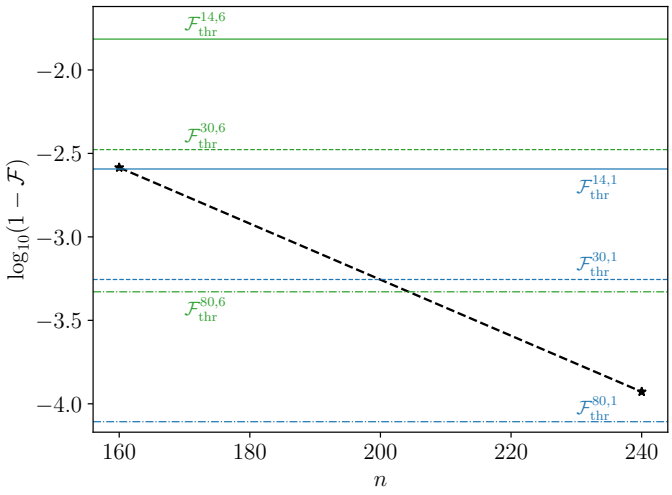

Figure 10. Unfaithfulness of `BAM:0066`'s Medium-High ($n_m = 240, 160$) and Low-Medium ($n_m = 160, 120$) Rh_{22} waveforms. The blue and green lines represent the accuracy tests $\mathcal{F}_{\rm thr}^{\rho,\epsilon^2}$ for different values of ρ (SNR) and ϵ^2.

4.2. Faithfulness analysis

In an attempt to give an overview of the accuracy of the waveform database, we compute the unfaithfulness of the (2,2) mode waveforms h_{22} between the highest and second highest resolutions, for the whole database. We use again the zero-detuned, high-power Advanced LIGO PSD [177]. The minimum frequency $f_{\rm min}$ employed in the integral of Eq. (18) corresponds to the initial frequency of each individual simulation.

The result of this analysis is summarized in Fig. 11, where $\bar{\mathcal{F}}$ is shown as a function of the number of orbits and different colors mark the microphysics scheme employed in each simulation. The unfaithfulness values are scattered on a wide range, but about 65% of the waveforms lay below the 1% level which is conventionally considered the accuracy threshold for detection purposes. Importantly, the dependence on the number of orbits (simulation length) is very weak and most of the simulations with ten or more orbits have $\bar{\mathcal{F}} < 0.01$. Several waveforms from multiple-orbits have $\bar{\mathcal{F}} \lesssim 10^{-4}$; according to the analysis in the previous section, these data can be considered faithful (suitable for parameter estimation) up to signal SNR of 30-80. We note that data with very few orbits (e.g. `THC:0019`, `BAM:0029`, and `BAM:0082`) show a remarkably low unfaithfulness. These simulations have a short inspiral and rather focus on the postmerger signal, which is not considered in this analysis. Hence, small $\bar{\mathcal{F}}$ is not necessarily an indication that these simulations are suitable for waveform modelling.

A faithfulness analysis for postmerger signals was recently presented by some of us in [31, 36]. There, we found average mismatches of $\sim 0.01 - 0.4$. The main source of uncertainty in the postmerger waveforms is the numerical resolution (see the above Section) and the impact of the resolution on the remnant's collapse.

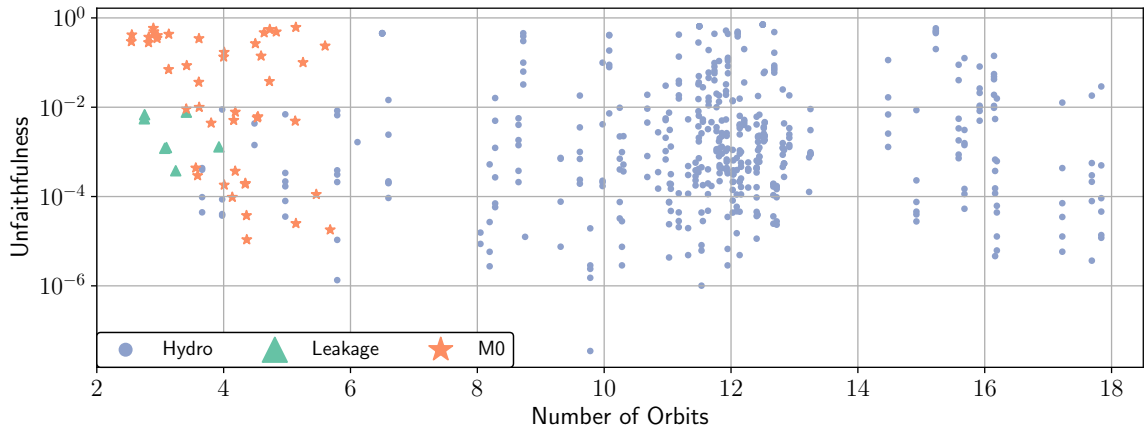

Figure 11. Unfaithfulness computed between the highest and second highest simulations h_{22} waveforms for every configuration of the database. The different colors and markers correspond to the microphysics scheme employed for each simulation.

Table 2. Updated fit coefficients for relevant merger and PM quantities.

$Q^{\rm fit}$	a_0	k	a_k^M	a_k^S	b_k^S	a_k^T	b_k^T	χ^2	Error	R^2
$A_{\rm mrg}/M$	0.55	1	5.27	0.31	-39.21	5.59×10^{-2}	-2.51×10^{-2}	0.113	2.6%	0.949
		2				1.00×10^{-6}	-2.00			
		3				0.12	11.09			
		4				6.79×10^{-5}	9.72			
$Mf_{\rm mrg}/\nu$	0.22	1	0.80	0.25	-1.99	4.85×10^{-2}	1.80	0.329	4.5%	0.925
		2				5.86×10^{-6}	599.99			
		3				0.1	7.80			
		4				1.86×10^{-4}	84.76			
Mf_2	8.99×10^{-2}	1	31.02	7.42×10^{-2}	29.99	2.94×10^{-2}	1.13	0.067	3.6%	0.958
		2				3.78×10^{-5}	-0.99			
		3				5.75×10^{-2}	39.99			
		4				2.77×10^{-4}	27.77			

Table 3. Updated fit coefficients for Mf_2 as a function of the NS radii $R_{1.4}$ and $R_{1.8}$.

	a_0	a_1	a_2	a_3	χ^2	Error	R^2
$Mf_2(R_{1.4}/M)$	0.24	-0.10	1.13×10^{-2}	-	0.55	5.9%	0.901
$Mf_2(R_{1.8}/M)$	0.23	-0.10	1.21×10^{-2}	-	0.31	4.5%	0.949
$Mf_2(R_{1.4}/M, R_{1.4}/R_{1.8})$	0.15	-0.11	1.38×10^{-2}	9.76×10^{-2}	0.31	4.5%	0.949
$Mf_2(R_{1.8}/M, R_{1.4}/R_{1.8})$	0.20	-0.10	1.22×10^{-2}	2.77×10^{-2}	0.30	4.4%	0.952

Table 4. Best fit coefficients for the luminosity peak. The last columns show the χ^2, the fit's relative standard deviation and the coefficient of determination R^2.

	k	p_{k10}	p_{k11}	p_{k20}	p_{k21}	p_{k30}	p_{k31}	χ^2	Error	R^2
$L_{\rm peak}/\nu$	1	2.28	7.59×10^{-1}	-17.74	-0.57	-17.47	4.58	2.23	12%	0.961
	2	-8.38×10^{-2}	9.61×10^{-3}	3.24×10^{-1}	-3.33×10^{-2}	13.91	10.10			
	3	-5.18×10^{-1}	14.64	-5.35	-50.54	11.61	-29.96			

5. Quasi-universal relations

As a first application of the database, we present in this section new EOS-insensitive relations for the merger and postmerger waveforms. Previous work found that several key quantities characterizing the merger dynamics depend on the unknown EOS mainly throughout the tidal parameters and have a very weak dependence on other details of the matter model, e.g., [27, 56, 144, 147, 179–181]. Similarly, the GW postmerger spectrum has robust features that can be captured within a few percent accuracy by tidal parameters and/or other properties of NS equilibria in EOS-insensitive way [25, 26, 31, 147–149]. These relations have some practical use in GW astronomy because they deliver accurate estimates for the peak luminosity [51, 144] and for the remnant properties [182–184] (see also [51] for a detailed review) and because they are the building blocks to develop NR-informed waveform models.

First, we consider the mass-rescaled GW amplitude and frequency at the moment of merger, $A_{22}^{\rm mrg}/M$ and $Mf_{22}^{\rm mrg}/\nu$, and update the fits developed in Ref. [31, 36, 180]. Following closely the fitting procedure of Ref. [36], we represent any quantity by the factorized function

$$Q^{\rm fit} = a_0 Q^M(X) Q^S(\hat{S}, X) Q^T(\kappa_2^T, X)\,, \tag{23}$$

where each factor Q^M, Q^S, Q^T accounts for the mass ratio in terms of $X = 1 - 4\nu$, spin corrections in terms of $\hat{S}$, and tidal effects in terms of κ_2^T. The first two factors are given by the linear polynomial expressions $Q^M = 1 + a_1^M X$, and $Q^S = 1 + p_1^S \hat{S}$, with $p_1^S = a_1^S(1 + b_1^S X)$. The last factor is instead a rational polynomial

$$Q^T = \frac{1 + p_1^T \kappa_2^T + p_2^T {\kappa_2^T}^2}{1 + p_3^T \kappa_2^T + p_4^T {\kappa_2^T}^2}\,, \tag{24}$$

with $p_i^T = a_i^T(1 + b_i^T X)$. The best fit parameters are shown in Tab. 2. The amplitude and frequency have 1σ errors of 2.6% and 4.6% respectively. We also obtain a χ^2 of ~ 0.126 for the former and ~ 0.329 for the latter.

Next, we use the public CoRe data on the emitted GW energy and extract the peak luminosity $L_{\rm peak}$ using Eq. (13). For binary black holes, this quantity does not depend on the mass scale and it is accurately described by the fits of Ref. [185]. For BNS, it has been studied in Ref. [144]. We propose the ansatz

$$L_{\rm peak}(\nu,\, \hat{S},\, \kappa_2^T)/\nu = L_{\rm peak}^{\rm BBH} \frac{1 + p_1(\nu,\, \hat{S})\kappa_2^T + p_2(\nu,\, \hat{S}){\kappa_2^T}^2}{(1 + [p_3(\nu,\, \hat{S})]^2 \kappa_2^T)^2}\,, \tag{25}$$

where $L_{\rm peak}^{\rm BBH}$ are the mass and spin dependent fits from Ref. [185] and

$$\begin{aligned} p_k(\nu,\, \hat{S}) &= p_{k1}(\hat{S})\nu + p_{k2}(\hat{S})\nu^2 + p_{k3}(\hat{S})\nu^3 \\ p_{kj}(\hat{S}) &= p_{kj0}\hat{S} + p_{kj1}\,. \end{aligned}$$

Note the scaling factor $1/\nu$ for $L_{\rm peak}$. By construction, the fit reduces to the BBH case for $\kappa_2^T \to 0$. The luminosity peak is calculated in geometric units; the conversion factor to CGS units is given by the Planck luminosity $L_P = c^5/G \approx 3.63 \times 10^{59}$ erg s^{-1}.

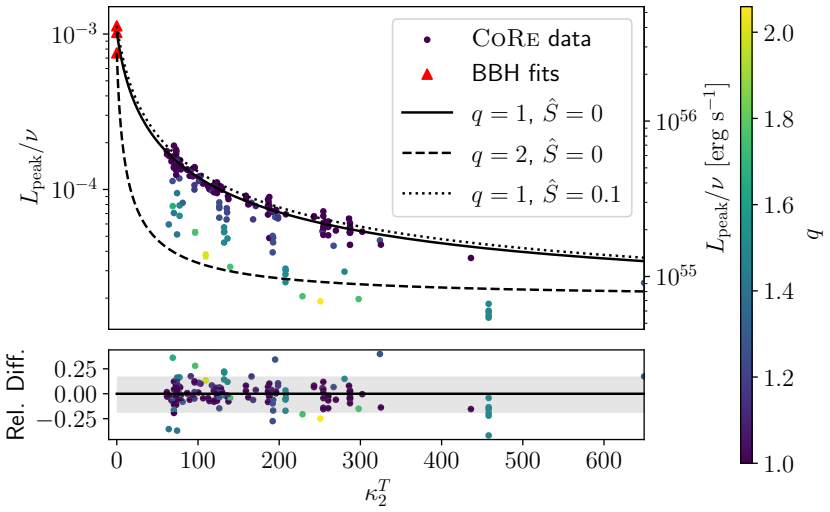

Figure 12. Luminosity peak data from the CoRe database. Black lines show the new fits developed for different mass ratio and spin configurations. The relative differences are shown in the bottom panel, where the gray shaded region marks the 90% credible region.

Figure 12 shows the best fit for $L_{\rm peak}/\nu$ and the CoRe data; the best fitting coefficients are reported in Tab. 4. The average 1σ deviation is about 17% over the entire dataset with less than a dozen of outliers. The peak luminosities for $q \sim 2$ BNS are the least accurately modelled (4 BNS configurations). The figure shows that the largest peak luminosities are reached by BNS with $\kappa_2^{\rm T} \lesssim 80$ that correspond to high-mass binaries and prompt collapse mergers. These events can reach peak luminosities of $\sim 10^{55}$ erg s^{-1}, about an order of magnitude less than binary black holes (of any mass). BNS mass ratios $q \gtrsim 1.5$ can lower $L_{\rm peak}$ of about an order of magnitude, while spins of magnitude ~ 0.1 do not significantly affect $L_{\rm peak}$. We stress that BNS with the largest peak luminosity do not correspond in general to the BNS that radiate the largest amount of energy because postmerger emission can radiate further energy [143, 144] (see also Fig. 5). We can set an upper limit to the total radiated GW energy from our dataset, obtaining $E_{\rm GW}^{\rm tot} \lesssim 0.676\ {\rm M}_\odot c^2$.

Finally, we illustrate the use of CoRe data to model postmerger GWs by discussing a fit of the postmerger's spectrum peak frequency f_2, e.g. [26, 27, 31, 36]. This peak frequency is a robust feature found in all NR simulations. Direct GW inference on f_2 can be used to constrain NS properties [30,32,148,149,182,183,186]. The peak frequency also enters as one of the central parameters in postmerger waveform models that will be employed in future for more sophisticated matched-filter analyses [187]. Following Ref. [36] we employ again Eq. (23) to fit the mass-rescaled Mf_2. The best fitting coefficients are presented in Table 2 and have a $\chi^2 \sim 0.07$. Figure 13 shows Mf_2 as a function of $\kappa_2^{\rm T}$ for selected values of mass ratio and spin. The 1σ error is below 4%; this

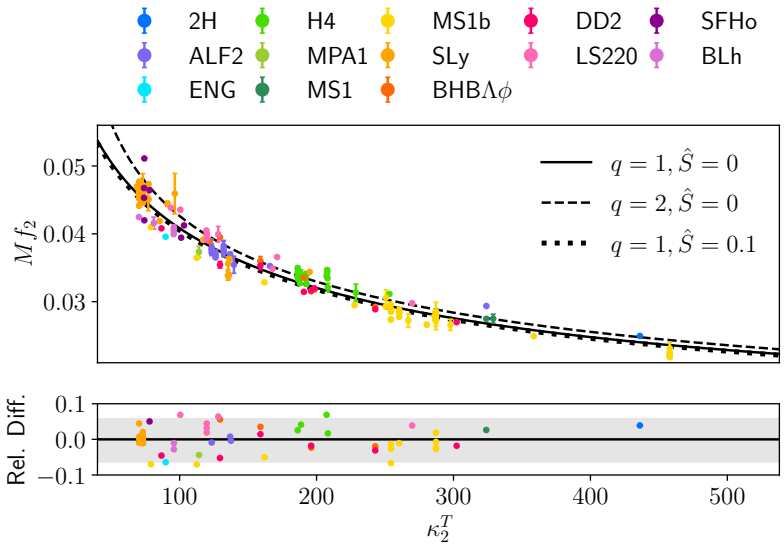

Figure 13. Quasi-universal relation of the post-merger peak frequency Mf_2 (mass rescaled) as a function of the tidal polarizability κ_2^T. Each point represents a simulation of the CoRe database with its corresponding EOS (in different colors). Black lines represent the updated Mf_2-fits (top panel). The relative differences are shown in the bottom panel, where the gray shaded region marks the 90% credible region.

precision is in principle sufficient for informative measurements of the NS mass-radius sequence. For example, using the EOS-insensitive relation between f_2 and the maximum density of an equilibrium non-rotating NS put forward in [149], it would be possible to determine the maximum density of an equilibrium non-rotating NS to ∼15% and the maximum mass $M_{\rm max}^{\rm TOV}$ to ∼12% with a single signal at the detectability threshold.

As a further illustration, we calibrate the EOS-insensitive relations (mass-rescaled) between f_2 and the NS radius [36, 188, 189]

$$
\begin{aligned}
Mf_2\left(\frac{R_X}{M}\right) &= a_0 + a_1\frac{R_X}{M} + a_2\left(\frac{R_X}{M}\right)^2 \\
Mf_2\left(\frac{R_X}{M}, \frac{R_{1.4}}{R_{1.8}}\right) &= a_0 + a_1\frac{R_X}{M} + a_2\left(\frac{R_X}{M}\right)^2 + a_3\frac{R_{1.4}}{R_{1.8}}\,,
\end{aligned}
\tag{26}
$$

where R_X is the equilibrium radius corresponding to a NS with mass $X = 1.4$, 1.8 $\mathrm{M}_\odot$. Figure 14 shows Mf_2 as function of $R_{1.4}$, $R_{1.8}$ and $R_{1.4}/R_{1.8}$. Best fit parameters are given in Table 3. Other features of the postmerger spectrum can be quantified in a similar way. We release reduced postmerger data and analysis scripts on the CoRe website.

6. Conclusion

We presented a new set of BNS simulations for the second release of the CoRe database, expanding it to 254 different binary configurations covering a wide parameter space.

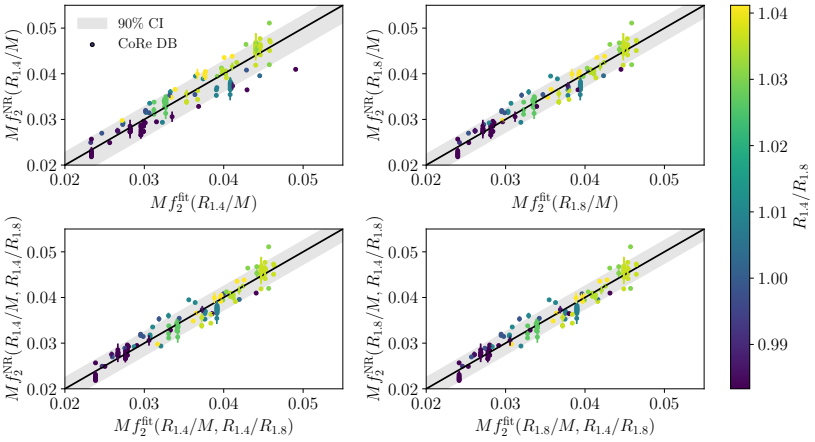

Figure 14. Quasi-universal relation of the post-merger peak frequency Mf_2 (mass rescaled) as a function of the NS radius $R_{1.4}$, $R_{1.8}$. Each point represents a simulation of the CoRe database with the different colors representing the ratio $R_{1.4}/R_{1.8}$. Each panel shows the different fit calibrations performed in [36]. The black line represents the case when $Mf_2^{\rm NR} = Mf_2^{\rm fit}$, whereas the gray area shows the 90% credibility level.

The new data includes BNS consistent with the GW events GW170817 [57] and GW190425 [64, 66]. Simulations were performed with a large number of EOSs, including several microphysical models [57, 61, 64]. Some simulations include the effects of neutrinos, either through the leakage scheme [104, 127, 190], or using the M0 approach [52, 104]. Turbulent viscosity is included in some models using the GRLES formalism [59, 106]. Finally, we include simulations produced using a new hybrid numerical flux scheme, EFL, that was introduced in [63] showing fourth order convergence and smaller phase errors than previous simulations using WENO schemes in BAM.

We described in detail the methodology we used to assess the overall accuracy of the waveforms and presented results for all the configurations in the database. The CoRe database waveform have typical unfaithfulness of less than 10^{-2}, some have unfaithfulness of less than 10^{-4}, so they are suitable for precision waveform modelling applications. However, to ensure the convergence and usability of the simulations, more extensive analysis is needed. As an example, we showed a full analysis of one of our simulations, `BAM:0066`, which showed a clear second order convergence and passed several accuracy tests.

Finally, as a first application of the CoRe database, we fitted phenomenological formulas for the merger amplitude, frequency, and GW luminosity. These fits are able to model the CoRe data with high accuracy ($< 5\%$ for the merger amplitude and frequency and 17% for the peak luminosity). We also recalibrated various quasi-universal relations between the post-merger peak frequency and the binary parameters, again finding deviations from the universal relations of only a few percent. These were used in [36] to construct the first complete inspiral, merger, and post-merger waveform

model for BNS.

We release the CoRe database to the community with the hope that it will enable future discoveries in GW astronomy. Potential applications include the development of new waveform models, the validation of data analysis pipelines and new numerical relativity codes, and the planning of future GW experiments. In the future, we plan to release new simulation data on a rolling basis, with data releases taking place at the time of the publication of the each paper.

Acknowledgments

AG, MB acknowledge partial support from the Deutsche Forschungsgemeinschaft (DFG) under Grant No. 406116891 within the Research Training Group RTG 2522/1. FZ, MB, SB, GD acknowledge support from the EU H2020 under ERC Starting Grant, no. BinGraSp-714626. DR acknowledges funding from the U.S. Department of Energy, Office of Science, Division of Nuclear Physics under Award Number(s) DE-SC0021177 and from the National Science Foundation under Grants No. PHY-2011725, PHY-2020275, PHY-2116686, and AST-2108467. SB acknowledges support from the Deutsche Forschungsgemeinschaft, DFG, project MEMI number BE 6301/2-1. BB acknowledges support from the Deutsche Forschungsgemeinschaft, DFG, Grant BR 2176/5-1. WT acknowledges funding from the National Science Foundation under Grants PHY-2011729 and PHY-2136036.

Numerical relativity simulations were performed at various supercomputing centers. ARA, a resource of Friedrich-Schiller-Universtät Jena supported in part by DFG grants INST 275/334-1 FUGG, INST 275/363-1 FUGG and EU H2020 BinGraSp-714626. The authors gratefully acknowledge the Gauss Centre for Supercomputing e.V. (`www.gauss-centre.eu`) for funding this project by providing computing time on the GCS Supercomputer SuperMUC at Leibniz Supercomputing Centre (`www.lrz.de`, Gauss projects pn29ba, pn56zo, pn68wi). The authors acknowledge the national High Performance Computing Center Stuttgart (HLRS) for providing access to the supercomputer HPE Apollo Hawk under the grant numbers GWanalysis/44189 and INTRHYGUE/44215. The authors gratefully acknowledge the computing time granted by the Resource Allocation Board and provided on the supercomputer Lise and Emmy as part of the NHR infrastructure, where resources were granted through the project bbp00049. Joliot-Curie at GENCI@CEA (PRACE-ra5202). Marconi at CINECA (ISCRA-B project HP10BMHFQQ, INF20_teongrav and INF21_teongrav allocation). Bridges, Bridges2, Comet, Expanse, Stampede2 (NSF XSEDE allocation TG-PHY160025), NSF/NCSA Blue Waters (NSF AWD-1811236), supercomputers. This research used resources of the National Energy Research Scientific Computing Center, a DOE Office of Science User Facility supported by the Office of Science of the U.S. Department of Energy under Contract No. DE-AC02-05CH11231.

The CoRe data are hosted on the `gitlab` server at TPI Jena. Data postprocessing was performed on the Virgo "Tullio" server at Torino supported by INFN.

References

[1] Mroue A H, Scheel M A, Szilagyi B, Pfeiffer H P, Boyle M et al. 2013 Phys.Rev.Lett. **111** 241104 (*Preprint* 1304.6077)

[2] Chu T, Fong H, Kumar P, Pfeiffer H P, Boyle M, Hemberger D A, Kidder L E, Scheel M A and Szilagyi B 2016 Class. Quant. Grav. **33** 165001 (*Preprint* 1512.06800)

[3] Boyle M et al. 2019 Class. Quant. Grav. **36** 195006 (*Preprint* 1904.04831)

[4] Healy J, Lousto C O, Zlochower Y and Campanelli M 2017 Class. Quant. Grav. **34** 224001 (*Preprint* 1703.03423)

[5] Healy J, Lousto C O, Lange J, O'Shaughnessy R, Zlochower Y and Campanelli M 2019 Phys. Rev. D **100** 024021 (*Preprint* 1901.02553)

[6] Healy J and Lousto C O 2020 Phys. Rev. D **102** 104018 (*Preprint* 2007.07910)

[7] Jani K, Healy J, Clark J A, London L, Laguna P and Shoemaker D 2016 Class. Quant. Grav. **33** 204001 (*Preprint* 1605.03204)

[8] Dietrich T, Radice D, Bernuzzi S, Zappa F, Perego A, Brügmann B, Chaurasia S V, Dudi R, Tichy W and Ujevic M 2018 Class. Quant. Grav. **35** 24LT01 (*Preprint* 1806.01625)

[9] Kiuchi K, Kawaguchi K, Kyutoku K, Sekiguchi Y, Shibata M and Taniguchi K 2017 Phys. Rev. **D96** 084060 (*Preprint* 1708.08926)

[10] Kiuchi K, Kyohei K, Kyutoku K, Sekiguchi Y and Shibata M 2019 (*Preprint* 1907.03790)

[11] Foucart F et al. 2019 Phys. Rev. D **99** 044008 (*Preprint* 1812.06988)

[12] Baiotti L, Damour T, Giacomazzo B, Nagar A and Rezzolla L 2011 Phys. Rev. **D84** 024017 (*Preprint* 1103.3874)

[13] Bernuzzi S, Nagar A, Thierfelder M and Brügmann B 2012 Phys.Rev. **D86** 044030 (*Preprint* 1205.3403)

[14] Bernuzzi S, Nagar A, Dietrich T and Damour T 2015 Phys.Rev.Lett. **114** 161103 (*Preprint* 1412.4553)

[15] Hinderer T et al. 2016 Phys. Rev. Lett. **116** 181101 (*Preprint* 1602.00599)

[16] Steinhoff J, Hinderer T, Buonanno A and Taracchini A 2016 Phys. Rev. **D94** 104028 (*Preprint* 1608.01907)

[17] Bernuzzi S and Dietrich T 2016 Phys. Rev. **D94** 064062 (*Preprint* 1604.07999)

[18] Dietrich T, Bernuzzi S and Tichy W 2017 Phys. Rev. **D96** 121501 (*Preprint* 1706.02969)

[19] Kawaguchi K, Kiuchi K, Kyutoku K, Sekiguchi Y, Shibata M and Taniguchi K 2018 Phys. Rev. **D97** 044044 (*Preprint* 1802.06518)

[20] Nagar A et al. 2018 Phys. Rev. **D98** 104052 (*Preprint* 1806.01772)

[21] Nagar A, Messina F, Rettegno P, Bini D, Damour T, Geralico A, Akcay S and Bernuzzi S 2019 Phys. Rev. **D99** 044007 (*Preprint* 1812.07923)

[22] Akcay S, Bernuzzi S, Messina F, Nagar A, Ortiz N and Rettegno P 2019 Phys. Rev. **D99** 044051 (*Preprint* 1812.02744)

[23] Isoyama S, Sturani R and Nakano H 2020 (*Preprint* 2012.01350)

[24] Gamba R, Akçay S, Bernuzzi S and Williams J 2022 Phys. Rev. D **106** 024020 (*Preprint* 2111.03675)

[25] Hotokezaka K, Kiuchi K, Kyutoku K, Muranushi T, Sekiguchi Y i et al. 2013 Phys.Rev. **D88** 044026 (*Preprint* 1307.5888)

[26] Bernuzzi S, Dietrich T and Nagar A 2015 Phys. Rev. Lett. **115** 091101 (*Preprint* 1504.01764)

[27] Bauswein A and Stergioulas N 2015 Phys. Rev. **D91** 124056 (*Preprint* 1502.03176)

[28] Clark J A, Bauswein A, Stergioulas N and Shoemaker D 2016 Class. Quant. Grav. **33** 085003 (*Preprint* 1509.08522)

[29] Easter P J, Lasky P D, Casey A R, Rezzolla L and Takami K 2019 Phys. Rev. D **100** 043005 (*Preprint* 1811.11183)

[30] Tsang K W, Dietrich T and Van Den Broeck C 2019 Phys. Rev. **D100** 044047 (*Preprint* 1907.02424)

[31] Breschi M, Bernuzzi S, Zappa F, Agathos M, Perego A, Radice D and Nagar A 2019 Phys. Rev. **D100** 104029 (*Preprint* 1908.11418)

[32] Easter P J, Ghonge S, Lasky P D, Casey A R, Clark J A, Vivanco F H and Chatziioannou K 2020 Phys. Rev. D **102** 043011 (*Preprint* 2006.04396)

[33] Soultanis T, Bauswein A and Stergioulas N 2022 Phys. Rev. D **105** 043020 (*Preprint* 2111.08353)

[34] Wijngaarden M, Chatziioannou K, Bauswein A, Clark J A and Cornish N J 2022 (*Preprint* 2202.09382)

[35] Whittaker T, East W E, Green S R, Lehner L and Yang H 2022 (*Preprint* 2201.06461)

[36] Breschi M, Bernuzzi S, Chakravarti K, Camilletti A, Prakash A and Perego A 2022 (*Preprint* 2205.09112)

[37] Abbott B P et al. (Virgo, LIGO Scientific) 2017 Astrophys. J. **851** L16 (*Preprint* 1710.09320)

[38] Abbott B P et al. (LIGO Scientific, Virgo) 2019 Phys. Rev. **X9** 011001 (*Preprint* 1805.11579)

[39] Abbott B P et al. (LIGO Scientific, Virgo) 2018 Phys. Rev. Lett. **121** 161101 (*Preprint* 1805.11581)

[40] Abbott B P et al. (LIGO Scientific, Virgo) 2020 Class. Quant. Grav. **37** 045006 (*Preprint* 1908.01012)

[41] Shibata M, Taniguchi K and Uryu K 2005 Phys. Rev. **D71** 084021 (*Preprint* gr-qc/0503119)

[42] Shibata M and Taniguchi K 2006 Phys.Rev. **D73** 064027 (*Preprint* astro-ph/0603145)

[43] Hotokezaka K, Kyutoku K, Okawa H, Shibata M and Kiuchi K 2011 Phys.Rev. **D83** 124008 (*Preprint* 1105.4370)

[44] Bernuzzi S, Dietrich T, Tichy W and Brügmann B 2014 Phys.Rev. **D89** 104021 (*Preprint* 1311.4443)

[45] Dietrich T, Ujevic M, Tichy W, Bernuzzi S and Brügmann B 2017 Phys. Rev. **D95** 024029 (*Preprint* 1607.06636)

[46] Dietrich T, Bernuzzi S, Ujevic M and Tichy W 2017 Phys. Rev. **D95** 044045 (*Preprint* 1611.07367)

[47] Dietrich T, Bernuzzi S, Brügmann B, Ujevic M and Tichy W 2018 Phys. Rev. **D97** 064002 (*Preprint* 1712.02992)

[48] Köppel S, Bovard L and Rezzolla L 2019 Astrophys. J. **872** L16 (*Preprint* 1901.09977)

[49] Baumgarte T W, Shapiro S L and Shibata M 2000 Astrophys. J. **528** L29 (*Preprint* astro-ph/9910565)

[50] Radice D, Bernuzzi S and Perego A 2020 Ann. Rev. Nucl. Part. Sci. **70** (*Preprint* 2002.03863)

[51] Bernuzzi S 2020 Gen. Rel. Grav. **52** 108 (*Preprint* 2004.06419)

[52] Radice D, Perego A, Hotokezaka K, Fromm S A, Bernuzzi S and Roberts L F 2018 Astrophys. J. **869** 130 (*Preprint* 1809.11161)

[53] Perego A, Bernuzzi S and Radice D 2019 Eur. Phys. J. **A55** 124 (*Preprint* 1903.07898)

[54] Endrizzi A, Perego A, Fabbri F M, Branca L, Radice D, Bernuzzi S, Giacomazzo B, Pederiva F and Lovato A 2020 Eur. Phys. J. A **56** 15 (*Preprint* 1908.04952)

[55] Poudel A, Tichy W, Brügmann B and Dietrich T 2020 Phys. Rev. D **102** 104014 (*Preprint* 2009.06617)

[56] Bernuzzi S et al. 2020 Mon. Not. Roy. Astron. Soc. (*Preprint* 2003.06015)

[57] Nedora V, Bernuzzi S, Radice D, Daszuta B, Endrizzi A, Perego A, Prakash A, Safarzadeh M, Schianchi F and Logoteta D 2021 Astrophys. J. **906** 98 (*Preprint* 2008.04333)

[58] Chaurasia S V, Dietrich T, Ujevic M, Hendriks K, Dudi R, Fabbri F M, Tichy W and Brügmann B 2020 Phys. Rev. D **102** 024087 (*Preprint* 2003.11901)

[59] Radice D 2020 Symmetry **12** 1249 (*Preprint* 2005.09002)

[60] Dudi R, Adhikari A, Brügmann B, Dietrich T, Hayashi K, Kawaguchi K, Kiuchi K, Kyutoku K, Shibata M and Tichy W 2021 (*Preprint* 2109.04063)

[61] Prakash A, Radice D, Logoteta D, Perego A, Nedora V, Bombaci I, Kashyap R, Bernuzzi S and Endrizzi A 2021 Phys. Rev. D **104** 083029 (*Preprint* 2106.07885)

[62] Ujevic M, Rashti A, Gieg H, Tichy W and Dietrich T 2022 (*Preprint* 2202.09343)

[63] Doulis G, Atteneder F, Bernuzzi S and Brügmann B 2022 Phys. Rev. D **106** 024001 (*Preprint* 2202.08839)
[64] Camilletti A, Chiesa L, Ricigliano G, Perego A, Lippold L C, Padamata S, Bernuzzi S, Radice D, Logoteta D and Guercilena F M 2022 (*Preprint* 2204.05336)
[65] Perego A, Radice D and Bernuzzi S 2017 Astrophys. J. **850** L37 (*Preprint* 1711.03982)
[66] Dudi R, Pannarale F, Dietrich T, Hannam M, Bernuzzi S, Ohme F and Bruegmann B 2018 (*Preprint* 1808.09749)
[67] Nagar A, Pratten G, Riemenschneider G and Gamba R 2019 (*Preprint* 1904.09550)
[68] Damour T and Nagar A 2010 Phys. Rev. **D81** 084016 (*Preprint* 0911.5041)
[69] Favata M 2014 Phys.Rev.Lett. **112** 101101 (*Preprint* 1310.8288)
[70] Reisswig C and Pollney D 2011 Class.Quant.Grav. **28** 195015 (*Preprint* 1006.1632)
[71] Damour T, Nagar A, Hannam M, Husa S and Brügmann B 2008 Phys. Rev. **D78** 044039 (*Preprint* 0803.3162)
[72] Baiotti L, Bernuzzi S, Corvino G, De Pietri R and Nagar A 2009 Phys. Rev. **D79** 024002 (*Preprint* 0808.4002)
[73] Damour T, Nagar A, Pollney D and Reisswig C 2012 Phys.Rev.Lett. **108** 131101 (*Preprint* 1110.2938)
[74] York James W J 1999 Phys.Rev.Lett. **82** 1350–1353 (*Preprint* gr-qc/9810051)
[75] Wilson J and Mathews G 1995 Phys.Rev.Lett. **75** 4161–4164
[76] Wilson J, Mathews G and Marronetti P 1996 Phys.Rev. **D54** 1317–1331 (*Preprint* gr-qc/9601017)
[77] Tichy W 2011 Phys.Rev. **D84** 024041 (*Preprint* 1107.1440)
[78] Tichy W 2012 Phys. Rev. D **86** 064024 (*Preprint* 1209.5336)
[79] Dietrich T, Moldenhauer N, Johnson-McDaniel N K, Bernuzzi S, Markakis C M, Brügmann B and Tichy W 2015 Phys. Rev. **D92** 124007 (*Preprint* 1507.07100)
[80] Tacik N et al. 2015 Phys. Rev. **D92** 124012 [Erratum: Phys. Rev.D94,no.4,049903(2016)] (*Preprint* 1508.06986)
[81] Tichy W, Rashti A, Dietrich T, Dudi R and Brügmann B 2019 Phys. Rev. **D100** 124046 (*Preprint* 1910.09690)
[82] Moldenhauer N, Markakis C M, Johnson-McDaniel N K, Tichy W and Brügmann B 2014 Phys. Rev. **D90** 084043 (*Preprint* 1408.4136)
[83] Tichy W 2009 Phys.Rev. **D80** 104034 (*Preprint* 0911.0973)
[84] Pfeiffer H P, Brown D A, Kidder L E, Lindblom L, Lovelace G and Scheel M A 2007 Class. Quant. Grav. **24** S59–S82 (*Preprint* gr-qc/0702106)
[85] Kyutoku K, Shibata M and Taniguchi K 2014 Phys. Rev. **D90** 064006 (*Preprint* 1405.6207)
[86] Gourgoulhon E, Grandclement P, Taniguchi K, Marck J A and Bonazzola S 2001 Phys.Rev. **D63** 064029 (*Preprint* gr-qc/0007028)
[87] Taniguchi K, Gourgoulhon E and Bonazzola S 2001 Phys. Rev. D **64** 064012 (*Preprint* gr-qc/0103041)
[88] Taniguchi K and Gourgoulhon E 2002 Phys. Rev. D **65** 044027 (*Preprint* astro-ph/0108086)
[89] Tichy W 2006 Phys.Rev. **D74** 084005 (*Preprint* gr-qc/0609087)
[90] Tichy W 2009 Class.Quant.Grav. **26** 175018 (*Preprint* 0908.0620)
[91] Nakamura T, Oohara K and Kojima Y 1987 Prog. Theor. Phys. Suppl. **90** 1–218
[92] Shibata M and Nakamura T 1995 Phys. Rev. **D52** 5428–5444
[93] Baumgarte T W and Shapiro S L 1999 Phys. Rev. **D59** 024007 (*Preprint* gr-qc/9810065)
[94] Brügmann B, Tichy W and Jansen N 2004 Phys. Rev. Lett. **92** 211101 (*Preprint* gr-qc/0312112)
[95] Bernuzzi S and Hilditch D 2010 Phys. Rev. **D81** 084003 (*Preprint* 0912.2920)
[96] Hilditch D, Bernuzzi S, Thierfelder M, Cao Z, Tichy W and Bruegmann B 2013 Phys. Rev. **D88** 084057 (*Preprint* 1212.2901)
[97] Font J A 2007 Living Rev. Rel. **11** 7
[98] Brügmann B, Gonzalez J A, Hannam M, Husa S, Sperhake U et al. 2008 Phys.Rev. **D77** 024027

(*Preprint* gr-qc/0610128)
[99] Thierfelder M, Bernuzzi S and Brügmann B 2011 Phys.Rev. **D84** 044012 (*Preprint* 1104.4751)
[100] Radice D and Rezzolla L 2012 Astron. Astrophys. **547** A26 (*Preprint* 1206.6502)
[101] Radice D, Rezzolla L and Galeazzi F 2014 Mon.Not.Roy.Astron.Soc. **437** L46–L50 (*Preprint* 1306.6052)
[102] Radice D, Rezzolla L and Galeazzi F 2014 Class.Quant.Grav. **31** 075012 (*Preprint* 1312.5004)
[103] Radice D, Rezzolla L and Galeazzi F 2015 ASP Conf. Ser. **498** 121–126 (*Preprint* 1502.00551)
[104] Radice D, Galeazzi F, Lippuner J, Roberts L F, Ott C D and Rezzolla L 2016 Mon. Not. Roy. Astron. Soc. **460** 3255–3271 (*Preprint* 1601.02426)
[105] Radice D, Bernuzzi S, Perego A and Haas R 2022 Mon. Not. Roy. Astron. Soc. **512** 1499–1521 (*Preprint* 2111.14858)
[106] Radice D 2017 Astrophys. J. **838** L2 (*Preprint* 1703.02046)
[107] Kiuchi K, Kyutoku K, Sekiguchi Y and Shibata M 2018 Phys. Rev. **D97** 124039 (*Preprint* 1710.01311)
[108] Goodale T, Allen G, Lanfermann G, Massó J, Radke T, Seidel E and Shalf J 2003 The Cactus framework and toolkit: Design and applications Vector and Parallel Processing – VECPAR'2002, 5th International Conference, Lecture Notes in Computer Science (Berlin: Springer)
[109] Loffler F et al. 2012 Class. Quant. Grav. **29** 115001 (*Preprint* 1111.3344)
[110] http://www.einsteintoolkit.org EinsteinToolkit: A Community Toolkit for Numerical Relativity
[111] Schnetter E, Hawley S H and Hawke I 2004 Class.Quant.Grav. **21** 1465–1488 (*Preprint* gr-qc/0310042)
[112] Berger M J and Colella P 1989 Journal of Computational Physics **82** 64–84
[113] Reisswig C, Haas R, Ott C D, Abdikamalov E, Mösta P, Pollney D and Schnetter E 2013 Phys. Rev. **D87** 064023 (*Preprint* 1212.1191)
[114] Read J S, Lackey B D, Owen B J and Friedman J L 2009 Phys. Rev. **D79** 124032 (*Preprint* 0812.2163)
[115] Banik S, Hempel M and Bandyopadhyay D 2014 Astrophys. J. Suppl. **214** 22 (*Preprint* 1404.6173)
[116] Bombaci I and Logoteta D 2018 Astron. Astrophys. **609** A128 (*Preprint* 1805.11846)
[117] Logoteta D, Perego A and Bombaci I 2021 Astron. Astrophys. **646** A55 (*Preprint* 2012.03599)
[118] Typel S, Ropke G, Klahn T, Blaschke D and Wolter H H 2010 Phys. Rev. **C81** 015803 (*Preprint* 0908.2344)
[119] Hempel M and Schaffner-Bielich J 2010 Nucl. Phys. **A837** 210–254 (*Preprint* 0911.4073)
[120] Lattimer J M and Swesty F D 1991 Nucl. Phys. **A535** 331–376
[121] Steiner A W, Hempel M and Fischer T 2013 Astrophys. J. **774** 17 (*Preprint* 1207.2184)
[122] Douchin F and Haensel P 2001 Astron. Astrophys. **380** 151–167 (*Preprint* astro-ph/0111092)
[123] Schneider A S, Roberts L F and Ott C D 2017 Phys. Rev. **C96** 065802 (*Preprint* 1707.01527)
[124] Alford M, Braby M, Paris M W and Reddy S 2005 Astrophys. J. **629** 969–978 (*Preprint* nucl-th/0411016)
[125] Radice D, Bernuzzi S, Del Pozzo W, Roberts L F and Ott C D 2017 Astrophys. J. **842** L10 (*Preprint* 1612.06429)
[126] Abbott B P et al. (Virgo, LIGO Scientific) 2017 Phys. Rev. Lett. **119** 161101 (*Preprint* 1710.05832)
[127] Galeazzi F, Kastaun W, Rezzolla L and Font J A 2013 Phys.Rev. **D88** 064009 (*Preprint* 1306.4953)
[128] Dieselhorst T, Cook W, Bernuzzi S and Radice D 2021 Symmetry **13** (*Preprint* 2109.02679)
[129] Bruenn S W 1985 Astrophys. J. Suppl. **58** 771–841
[130] Ruffert M H, Janka H T and Schäfer G 1996 Astron. Astrophys. **311** 532–566 (*Preprint* astro-ph/9509006)

[131] Burrows A, Reddy S and Thompson T A 2006 Nucl. Phys. **A777** 356–394 (*Preprint* astro-ph/0404432)
[132] Shapiro S L and Teukolsky S A 1983 Black holes, white dwarfs, and neutron stars: The physics of compact objects (New York, USA: Wiley) ISBN 978-0-471-87316-7
[133] Gold R, Bernuzzi S, Thierfelder M, Brügmann B and Pretorius F 2012 Phys.Rev. **D86** 121501 (*Preprint* 1109.5128)
[134] Chaurasia S V, Dietrich T, Johnson-McDaniel N K, Ujevic M, Tichy W and Brügmann B 2018 Phys. Rev. D **98** 104005 (*Preprint* 1807.06857)
[135] Damour T 2001 Phys. Rev. **D64** 124013 (*Preprint* gr-qc/0103018)
[136] Campanelli M, Lousto C O and Zlochower Y 2006 Phys. Rev. **D74** 084023 (*Preprint* astro-ph/0608275)
[137] Bauswein A, Baumgarte T and Janka H T 2013 Phys.Rev.Lett. **111** 131101 (*Preprint* 1307.5191)
[138] Kashyap R et al. 2022 Phys. Rev. D **105** 103022 (*Preprint* 2111.05183)
[139] Perego A, Logoteta D, Radice D, Bernuzzi S, Kashyap R, Das A, Padamata S and Prakash A 2022 Phys. Rev. Lett. **129** 032701 (*Preprint* 2112.05864)
[140] Bauswein A, Blacker S, Vijayan V, Stergioulas N, Chatziioannou K, Clark J A, Bastian N U F, Blaschke D B, Cierniak M and Fischer T 2020 Phys. Rev. Lett. **125** 141103 (*Preprint* 2004.00846)
[141] Tootle S D, Papenfort L J, Most E R and Rezzolla L 2021 Astrophys. J. Lett. **922** L19 (*Preprint* 2109.00940)
[142] Kölsch M, Dietrich T, Ujevic M and Bruegmann B 2022 Phys. Rev. D **106** 044026 (*Preprint* 2112.11851)
[143] Bernuzzi S, Radice D, Ott C D, Roberts L F, Moesta P and Galeazzi F 2016 Phys. Rev. **D94** 024023 (*Preprint* 1512.06397)
[144] Zappa F, Bernuzzi S, Radice D, Perego A and Dietrich T 2018 Phys. Rev. Lett. **120** 111101 (*Preprint* 1712.04267)
[145] Shibata M and Uryu K 2002 Prog. Theor. Phys. **107** 265 (*Preprint* gr-qc/0203037)
[146] Stergioulas N, Bauswein A, Zagkouris K and Janka H T 2011 Mon.Not.Roy.Astron.Soc. **418** 427 (*Preprint* 1105.0368)
[147] Bauswein A and Janka H T 2012 Phys.Rev.Lett. **108** 011101 (*Preprint* 1106.1616)
[148] Takami K, Rezzolla L and Baiotti L 2014 Phys.Rev.Lett. **113** 091104 (*Preprint* 1403.5672)
[149] Breschi M, Bernuzzi S, Godzieba D, Perego A and Radice D 2022 Phys. Rev. Lett. **128** 161102 (*Preprint* 2110.06957)
[150] Zappa F, Bernuzzi S, Radice D and Perego A 2022 (*Preprint* 2210.11491)
[151] Sekiguchi Y, Kiuchi K, Kyutoku K and Shibata M 2011 Phys.Rev.Lett. **107** 051102 (*Preprint* 1105.2125)
[152] Wanajo S, Sekiguchi Y, Nishimura N, Kiuchi K, Kyutoku K and Shibata M 2014 Astrophys. J. **789** L39 (*Preprint* 1402.7317)
[153] Sekiguchi Y, Kiuchi K, Kyutoku K and Shibata M 2015 Phys.Rev. **D91** 064059 (*Preprint* 1502.06660)
[154] Foucart F, O'Connor E, Roberts L, Kidder L E, Pfeiffer H P and Scheel M A 2016 Phys. Rev. **D94** 123016 (*Preprint* 1607.07450)
[155] Nedora V, Schianchi F, Bernuzzi S, Radice D, Daszuta B, Endrizzi A, Perego A, Prakash A and Zappa F 2022 Class. Quant. Grav. **39** 015008 (*Preprint* 2011.11110)
[156] Lehner L, Liebling S L, Palenzuela C, Caballero O L, O'Connor E, Anderson M and Neilsen D 2016 Class. Quant. Grav. **33** 184002 (*Preprint* 1603.00501)
[157] Fujibayashi S, Kiuchi K, Nishimura N, Sekiguchi Y and Shibata M 2018 Astrophys. J. **860** 64 (*Preprint* 1711.02093)
[158] Fujibayashi S, Shibata M, Wanajo S, Kiuchi K, Kyutoku K and Sekiguchi Y 2020 Phys. Rev. D **101** 083029 (*Preprint* 2001.04467)
[159] Radice D, Perego A, Bernuzzi S and Zhang B 2018 Mon. Not. Roy. Astron. Soc. **481** 3670–3682

(*Preprint* 1803.10865)
[160] Chandrasekhar S 1970 Astrophys. J. **161** 561
[161] Friedman J L and Schutz B F 1978 Astrophys. J. **221** 937–957
[162] East W E, Paschalidis V, Pretorius F and Shapiro S L 2016 Phys. Rev. **D93** 024011 (*Preprint* 1511.01093)
[163] Radice D, Bernuzzi S and Ott C D 2016 Phys. Rev. **D94** 064011 (*Preprint* 1603.05726)
[164] Bernuzzi S, Thierfelder M and Brügmann B 2012 Phys.Rev. **D85** 104030 (*Preprint* 1109.3611)
[165] Cutler C and Flanagan E E 1994 Phys.Rev. **D49** 2658–2697 (*Preprint* gr-qc/9402014)
[166] Apostolatos T A 1995 Phys. Rev. **D52** 605–620
[167] Owen B J 1996 Phys. Rev. **D53** 6749–6761 (*Preprint* gr-qc/9511032)
[168] Damour T, Iyer B R and Sathyaprakash B S 1998 Phys. Rev. **D57** 885–907 (*Preprint* gr-qc/9708034)
[169] Lindblom L, Owen B J and Brown D A 2008 Phys.Rev. **D78** 124020 (*Preprint* 0809.3844)
[170] Lindblom L 2009 Phys.Rev. **D80** 064019 (*Preprint* 0907.0457)
[171] Lindblom L, Baker J G and Owen B J 2010 Phys.Rev. **D82** 084020 (*Preprint* 1008.1803)
[172] Damour T, Nagar A and Trias M 2011 Phys. Rev. **D83** 024006 (*Preprint* 1009.5998)
[173] Flanagan E E and Hughes S A 1998 Phys. Rev. **D57** 4535–4565 (*Preprint* gr-qc/9701039)
[174] Gamba R, Breschi M, Bernuzzi S, Agathos M and Nagar A 2021 Phys. Rev. D **103** 124015 (*Preprint* 2009.08467)
[175] Lousto C O, Nakano H, Zlochower Y and Campanelli M 2010 Phys.Rev. **D82** 104057 (*Preprint* 1008.4360)
[176] Reisswig C, Bishop N T, Pollney D and Szilagyi B 2010 Class. Quant. Grav. **27** 075014 (*Preprint* 0912.1285)
[177] Updated Advanced LIGO sensitivity design curve https://dcc.ligo.org/LIGO-T1800044/public
[178] Breschi M, Gamba R and Bernuzzi S 2021 Phys. Rev. D **104** 042001 (*Preprint* 2102.00017)
[179] Read J S, Baiotti L, Creighton J D E, Friedman J L, Giacomazzo B et al. 2013 Phys.Rev. **D88** 044042 (*Preprint* 1306.4065)
[180] Bernuzzi S, Nagar A, Balmelli S, Dietrich T and Ujevic M 2014 Phys.Rev.Lett. **112** 201101 (*Preprint* 1402.6244)
[181] Rezzolla L and Takami K 2016 Phys. Rev. **D93** 124051 (*Preprint* 1604.00246)
[182] Bauswein A, Janka H, Hebeler K and Schwenk A 2012 Phys.Rev. **D86** 063001 (*Preprint* 1204.1888)
[183] Bauswein A, Stergioulas N and Janka H T 2014 Phys.Rev. **D90** 023002 (*Preprint* 1403.5301)
[184] Agathos M, Zappa F, Bernuzzi S, Perego A, Breschi M and Radice D 2020 Phys. Rev. **D101** 044006 (*Preprint* 1908.05442)
[185] Keitel D et al. 2017 Phys. Rev. **D96** 024006 (*Preprint* 1612.09566)
[186] Chatziioannou K, Clark J A, Bauswein A, Millhouse M, Littenberg T B and Cornish N 2017 Phys. Rev. **D96** 124035 (*Preprint* 1711.00040)
[187] Breschi M, Gamba R, Borhanian S, Carullo G and Bernuzzi S 2022 (*Preprint* 2205.09979)
[188] Most E R and Raithel C A 2021 Phys. Rev. D **104** 124012 (*Preprint* 2107.06804)
[189] Raithel C A and Most E R 2022 (*Preprint* 2201.03594)
[190] Neilsen D, Liebling S L, Anderson M, Lehner L, O'Connor E et al. 2014 Phys.Rev. **D89** 104029 (*Preprint* 1403.3680)

Appendix A. Public CoRe Database

The simulation data discussed in this work is publicly available at

https://core-gitlfs.tpi.uni-jena.de/

The database metadata are summarized in the repo `core-database-index`, which contains a `json` file with the main properties of the available simulations and the different runs. A repository is associated to one distinct physical binary and contains folders for the different runs performed. For each run, we release a complete metadata file and a HDF5 file with the multipolar waveform for both $\psi_{\ell m}$ and $h_{\ell m}$ at different extraction radii and the energetics.

Appendix B. `watpy`: Waveform Analysis Tools in Python

The repository

`https://git.tpi.uni-jena.de/core/watpy`

provides classes to work with the CoRe waveforms and tutorials. It is also available via `PyPI`

`https://pypi.org/project/core-watpy/`.

The code includes two main modules. The `coredb` module contains tools to download and upload NR simulation data, menage the metadata of the simulations, visualize statistics of the database, and work with the HDF5 files provided in the CoRe website. The `wave` module provides methods for the visualization and the analysis of (multipolar) NR outputs, i.e. Weyl curvature and GW strain. `watpy` is compatible with NR files from BAM, Cactus/Einstein Toolkit (WhiskyTHC/FreeTHC) and the CoRe database.

Appendix C. Merger and postmerger fit data

The data and scripts employed for the development of the fits presented in this work, can be found in

`https://doi.org/10.5281/zenodo.7253784`

Appendix D. `THC`

`THC` is open source and publicly available At

`https://bitbucket.org/FreeTHC/workspace/projects/THC`

A tutorial, microphysics tables, and example parfiles are available at

`http://personal.psu.edu/~dur566/whiskythc.html`